Materials Today Bio 16 (2022) 100347

Contents lists available at ScienceDirect

Materials Today Bio

journal homepage: www.journals.elsevier.com/materials-today-bio

Accelerating the excisional wound closure by using the patterned microstructural nanofibrous mats/gentamicin-loaded hydrogel composite scaffold

Nur Adila Mohd Razali, Wei-Chih Lin *

Department of Mechanical and Electro-mechanical Engineering, National Sun Yat-sen University, 80424, Taiwan

ARTICLE INFO

Keywords:
Micropattern nanofibre
Topographical effect
Nanofibre/hydrogel scaffold
Tissue regeneration
Wound healing

ABSTRACT

Ideal artificial tissue scaffolds should provide an in vitro microenvironment comparable to native human skin tissue to direct cell functions, regulate tissue homeostasis, and promote tissue regeneration. A sandwich-like composite scaffold consisting of a hydrogel layer and two aligned nanofibre layers was fabricated and applied as a wound-healing dressing. Gentamicin was preloaded into the hydrogel middle layer and naturally released for antibacterial activity during the healing period. Nanofibrous layers embedded on the top and bottom surfaces of the hydrogel improved the tensile strength fivefold (1560 kPa and 465% strain) while serving as a diffusion barrier to reduce the gentamicin initial burst release (30%–15%). Inspired by the extracellular matrix (ECM), the surface of nanofibre top layer was patterned with triangular microarrays using micro-moulding approach to reflect the multidimensional structure of ECM. Biocompatibility of the scaffold is proven from cytotoxicity and haemolysis studies. Fibroblast cells revealed a highly elongated and consistent alignment modulated by the micropatterned fibrous layer and directed their migration towards the wound area. Excisional wounds treated with the scaffold promoted 97.49% wound closure with low inflammation and rapid re-epithelialization and angiogenesis. This scaffold, with its tailored functionality capable of accelerating wound healing, has high potential in tissue engineering applications.

1. Introduction

Significant effort has been expended on the development of polymeric biomaterials that can meet the demands of a wide range of tissue engineering application. Polymeric biomaterials, either natural or synthetic, can be processed into membranes, nanoparticles, hydrogels, and fibres to construct artificial scaffolds that resemble the natural tissue microenvironment and provide mechanical and biological support for cell growth and subsequent tissue development. Fibre/hydrogel composites, inspired by the extracellular matrix (ECM) structure consisting of incorporated fibrous protein networks within a gelatinous polysaccharide ground substance, have been developed as formulations for biomimetic scaffolds to achieve true mimicry of the ECM architecture. Approaches taken for integration of the nanofibres and hydrogels [1,2] have included combinations of electrospinning and electrospraying techniques [3,4], blending of nanofibres in a hydrogel solution before polymerisation [5–7], and layer-by-layer assembly [8–10]. The nanofibres act as the reinforcing fillers which can greatly improve the low mechanical stability of the hydrogel [11–14]. For instance, fragment boron nitride nanofibres (BNNFs) prepared by freeze-drying and pyrolysis were dispersed in polyvinyl alcohol (PVA) to form BNNF/PVA composite hydrogels using a cyclic freezing-thawing treatment [15]. The compressive and tensile strength of the BNNF/PVA composites were increased significantly with the addition of even a small weight percentage of BNNF nanofibres. Previous work has shown that the addition of 0.5 wt% BNNFs increased the compressive strength by 252%, and that 1 wt% BNNFs increased the tensile strength by 87.8%. Another study used random or aligned gelatine nanofibres, infiltrated in an alginate hydrogel to create a single layer composite structures, as well as stacked in multilayer laminates with defined fibre orientations [12]. The reinforcement of a single, aligned nanofibre layer improved the mechanical properties by up to two orders of magnitude and showed inherently anisotropic mechanical behaviour, whereas multilayer laminates stacked in different fibre orientations doubled the toughness, over the hydrogel alone. The current recommendation upon integration of nanofibre and hydrogel is to integrate nanofibres into the hydrogel as laminated

* Corresponding author.
E-mail address: wc.lin@mail.nsysu.edu.tw (W.-C. Lin).

https://doi.org/10.1016/j.mtbio.2022.100347
Received 20 April 2022; Received in revised form 10 June 2022; Accepted 27 June 2022
Available online 30 June 2022

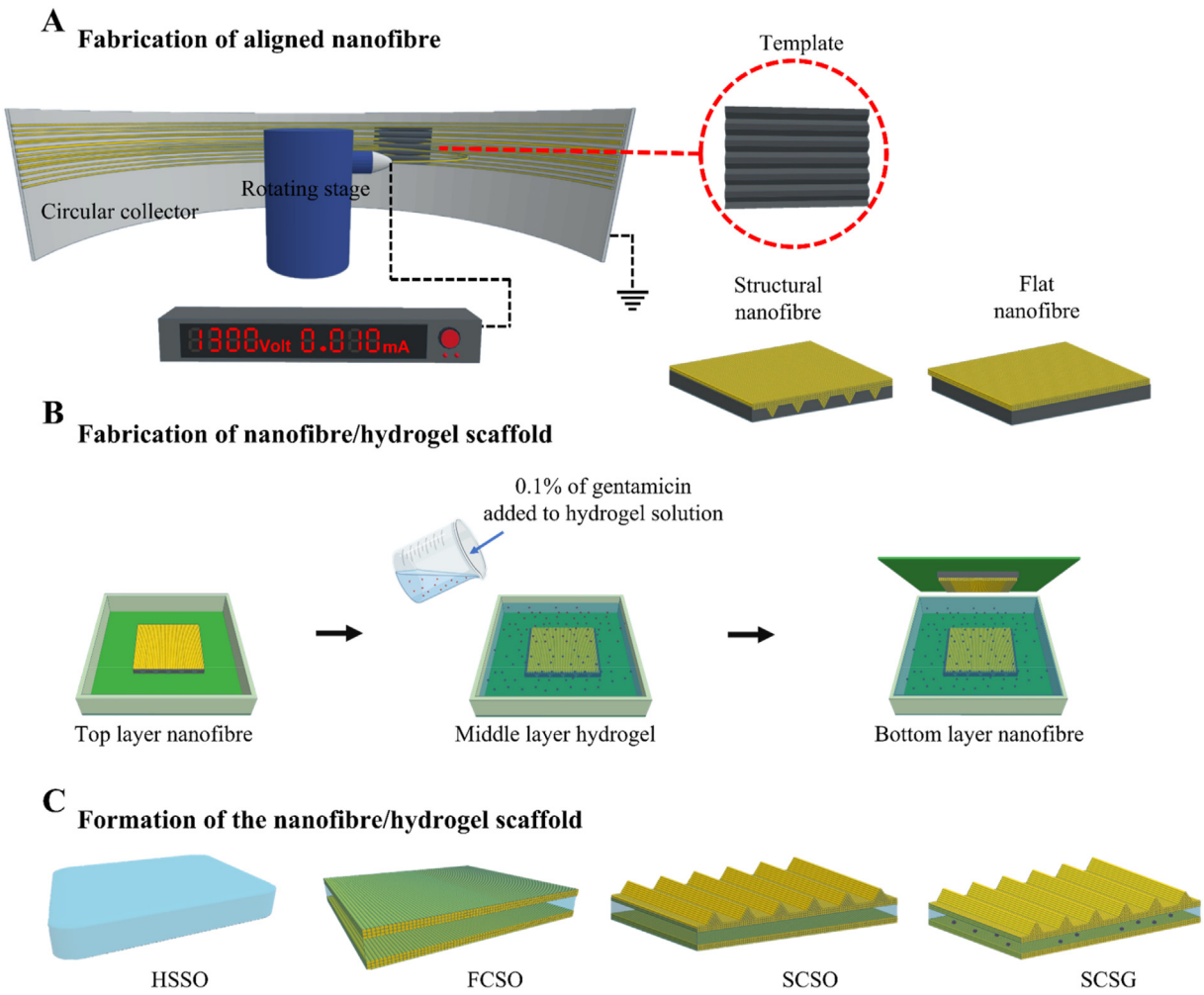

Fig. 1. Schematic of the composite scaffold fabrication processes. (A) Fabrication of the aligned nanofibre meshes with flat and structural surfaces. A patterned template with triangular prism gratings was mounted onto the collector of the centrifugal electrospinning machine to generate a triangular prism microarray on the surface of the nanofibre mesh. A flat template was used to fabricate the flat nanofibre mesh. (B) The hydrogel precursor solution, with or without added gentamicin sulphate, was casted onto the structural nanofibre mesh, followed by layering a flat nanofibre mesh as a bottom liner. (C) Four types of scaffolds were fabricated: a pure hydrogel (HSSO), a composite scaffold with flat topography (FCSO), a composite scaffold with structural topography (SCSO) and a gentamicin-loaded composite scaffold with structural topography (SCSG).

structures rather than incorporating fragments fibres directly into the hydrogel, as the laminated structures have greater mechanical strength due to the transversely isotropic material of the structure [16]. Apart from serving as a reinforcing agent, the laminated structure also induces cell signalling components, as the fibres are structurally interconnected into native ECM [17].

The beneficial properties of combining nanofibres and hydrogels are particularly noticeable in drug delivery applications. Nanofibres and hydrogels, by virtue of their high loading efficiencies, are widely used for the delivery of bioactive molecules. However, as a consequence of diffusion-based release and the homogeneity of the encapsulated drug, the drug release mechanism from the nanofibre and hydrogel are difficult to control [18,19]. By contrast, blended or monolithic matrix materials can provide extended and sustained release, although burst release is still difficult to avoid [20,21]. A laminated nanofibre layer can resolve this issue by serving as an additional diffusion barrier that slows the diffusion of drug molecules and reduces the burst release from the hydrogel [8,9,22]. Previous research that examined poly (ethylene glycol)-poly (ε-caprolactone) diacrylate (PEGPCL) hydrogels sandwiched between polycaprolactone (PCL) fibre mats reported that the burst release was reduced from 20% to 7% and that loaded bovine serum albumin (BSA) showed a linear release and an extended release duration [23]. The release properties of adenosine triphosphate (ATP) from laminated multilayer PCL-alginate composites suggest that multiple drug release at different rates and time can be achieved by discrete drug encapsulation in designated layers [22]. When compared to the release from the deeper layers in the meshes, ATP contained in the upper layer released at a faster rate with a significantly higher burst release in a shorter time.

Skin tissue engineering for effective wound healing requires biomaterial scaffolds with appropriate biophysical signals that can support tissue regeneration and provide instructive cues during tissue repair. During wound healing, biophysical signals activate precise intracellular signalling pathways that facilitate cell spreading and intrinsic contractility by regulating cell behaviour [24–27]. Previous research has demonstrated that generating microstructures provides control over the initial cell attachment and that these microstructures become the main focal point for cell growth. The flexibility of the cell cytoskeleton on the microstructures is limited due to strong geometrical constraints, which cause the cells to elongate with long filopodial protrusions along the microstructure rather than to expand [28]. These microstructures are key parameters that guide cell polarisation, motility [29], and migration; consequently, these cell-scaffold interactions may accelerate epidermal wound healing. In addition, the incorporation of bioactive molecules can induce specific cellular and biological functions to further improve the

wound healing process. For example, wound inflammation caused by biofilm formation and bacterial colonisation at the wound site can be prevented by incorporating antibacterial compounds, such as gentamicin [30–32], vancomycin [33,34], and silver nanoparticles, to prevent prolonged inflammation that leads to impaired healing.

In the present study, a composite design principle is used to integrate polycaprolactone (PCL) nanofibres and poly di(ethylene glycol) methyl ether methacrylate-oligo (ethylene glycol) methyl ether methacrylate ($PMEO_2MA$-OEGMA) hydrogel to fabricate a composite scaffold for use as a wound dressing. The composite scaffold was designed as three layers: a PCL nanofibre top layer, the $PMEO_2MA$-OEGMA hydrogel middle layer, and a PCL nanofibre bottom layer. The topographic surface of the nanofibre top layer was further modified with an appropriate surface microstructure to replicate the 3D hierarchical multiscale topography of the ECM architecture, as the regulation of cellular morphology and migration are important features of the wound-healing process. The hydrogel was endowed with antibacterial activity by blending gentamicin sulphate into the hydrogel solution prior to polymerisation as the gentamicin is commonly used in the treatment of superficial skin infections. The influence of the integrated nanofibres on the physical, mechanical, and swelling properties of the scaffold were assessed by comparison with the pure hydrogel. The potential applicability of these composite scaffolds as wound dressings for rapid healing was also evaluated in vitro and in vivo.

2. Materials and methods

As illustrated in Fig. 1, the nanofibre/hydrogel composite scaffolds were fabricated by a centrifugal electrospinning and casting technique. The first fabrication step was direct spinning of the PCL solution onto the topographically patterned template to generate spatially defined triangular prism microstructure arrays on the nanofibre surface. The structural integrity of the generated microstructures was maintained in the second step by casting the hydrogel solution onto the fabricated structural nanofibre mesh without removing the fibres from the template. The final step involved layering a flat nanofibre mesh on top of the hydrogel solution to form a sandwich-like nanofibre/hydrogel composite scaffold. This design method using a layer-by-layer arrangement allows for homogeneous dispersion of continuous nanofibre layers during integration with hydrogel, and the layout can be easily adjusted to match any specific requirements. Four different types of scaffolds with enhanced biofunctionalities were fabricated to explore the effects of structural topography and gentamicin loading on acceleration of the wound-healing process.

2.1. Fabrication of aligned polycaprolactone (PCL) nanofibre mesh with structural and flat surface topography

A centrifugal electrospinning machine was utilised to fabricate nanofibre meshes with a highly aligned fibre arrangement, as cell behaviours are more strongly regulated by aligned fibres than by random fibres [35,36]. PCL-based polyurethane synthesised according to our previous study [37] was used to fabricate the top and bottom nanofibre layers. The PCL was dissolved in hexafluoroisopropanol (HFIP, Sigma Aldrich, Taiwan) at 20% (w/w) and stirred for 24 h to obtain a homogeneously dispersed solution. A 2 ml volume of the solution was loaded into a syringe fitted with a 25-gauge blunt needle (0.26 mm diameter) and fixed on a rotating stage with a 10 cm vertical distance between the needle and circular collector. The spinning process was carried out with 8 kV applied voltage and rotation at 1300 rpm. The triangular microstructural microarrays on the surface of the nanofibre layer was created using a template with triangular profile gratings as template collector. This template was fabricated using a standard microfabrication process [28] and mounted onto the collector during the spinning process. A similar template, but with a flat surface, was used to fabricate a nanofibre layer with a flat surface topography.

Table 1
Configurations of the fabricated scaffolds and their corresponding sample codes.

Sample	Configuration	Gentamicin (wt%)	Sample code
Hydrogel	Single layer	–	HSSO
Flat composite	Composite layers	–	FCSO
Structural composite	Composite layers	–	SCSO
Hydrogel	Single layer	0.1	HSSG
Flat composite	Composite layers	0.1	FCSG
Structural composite	Composite layers	0.1	SCSG

2.2. Preparation of $PMEO_2MA$-OEGMA hydrogel precursor solution

Briefly, the hydrogel precursor solution was prepared using di(ethylene glycol) methyl ether methacrylate (MEO_2MA, Sigma Aldrich, Taiwan) and oligo (ethylene glycol) methyl ether methacrylate (OEGMA, Sigma Aldrich, Taiwan) monomers mixed at a 9:1 M ratio to achieve a lower critical solution temperature near to body temperature (37 °C). The polymers were cross-linked with di(ethylene glycol) di methacrylate (DEGDMA, Sigma Aldrich, Taiwan) using water/ethanol (1/1) as the solvent. Then, ammonium persulphate (APS, Wako Pure Chemical Industries, Japan) and tetramethyl ethylenediamine (TEMED, Wako Pure Chemical Industries, Japan) were added to initiate and activate the polymerisation, with all ratios kept at 0.5 wt% of the total polymer amount. Subsequently, 0.1 wt% of gentamicin sulphate (GS, Sigma Aldrich, Taiwan) was added to the solution and the mixture was stirred and sonicated for 3 min to form a homogeneous solution. A similar hydrogel solution without added gentamicin was also prepared by this method.

2.3. Fabrication of the nanofibre/hydrogel composite scaffolds

The deposited nanofibre mesh was left on the patterned template to maintain the structural integrity if the generated microstructures, and the prepared hydrogel precursor solution was directly poured onto the fibres until completely infiltrated. A flat nanofibre mesh was then layered as a bottom liner for the composite scaffold to offer structural support and dimensional stability [38] and allowed to cross-linked to form a sandwich-like composite scaffold. The scaffold was cross-linked at 4 °C for at least 4 h and then washed thoroughly with ultrapure water and ethanol to remove unreacted materials. The fabricated scaffold was then dried and kept in a vacuum desiccator until further analysis. Pure hydrogel scaffold without nanofibre layers was also fabricated to serve as control in all analyses. Table 1 shows the fabricated scaffold configurations and their respective sample codes used in this study.

2.4. Characterisation: morphological, porosity, swelling degree and mechanical

The morphology of the fabricated scaffolds was characterised by scanning electron microscopy (SEM, JSM638, JEOL) under 10 kV accelerating voltage. All samples were coated with a thin gold layer before observation. The efficiency of the applied fabrication method was evaluated using ImageJ software to measure the structural dimensions of the scaffolds, including the diameter and alignment of the nanofibres and the size of the replicated structural arrays.

Porosity can influence the mechanical and biological performance of the fabricated scaffolds thus the porosity measurement of nanofibre mesh, hydrogel and composite scaffolds were done. The porosity of nanofibre mesh is calculated using equation (1) [39]:

$$Porosity(\%) = \left(1 - \frac{\rho_{apparent}}{\rho_{bulk}}\right) \times 100\% \quad (1)$$

where $\rho_{apparent}$ and ρ_{bulk} is the density of apparent nanofibre and bulk material respectively. For the hydrogel and composite scaffold, the porosity is calculated using liquid displacement method. The fabricated

scaffold was added to a known volume of ethanol for 24 h to ensure all pores are completely filled with ethanol. The resulting volume at this stage was measured. Then, the scaffold was removed, and the remaining volume was measured. The amount of ethanol lost is equivalent to the void volume. The porosity of the fabricated scaffold is calculated by equation (2) [39]:

$$Porosity\ (\%) = \frac{V_3}{V_3 + V_2 + V_1} \tag{2}$$

where V_1, V_2, and V_3 is the initial volume of ethanol, the volume of ethanol with scaffold, and the final volume of ethanol after scaffold was removed.

The swelling degree of the fabricated scaffold was determined by gravimetric measurement. Dried samples were pre-weighed and immersed in ultrapure water at 37 °C. The mass of the samples was recorded at regular intervals throughout the swelling process until swelling equilibrium was achieved. The swelling ratio (S_t) was calculated using equation (3):

$$S_t = \frac{W_t - W_d}{W_d} \tag{3}$$

where W_d and W_t represent the weights of the dry and wet scaffold, respectively.

The tensile properties of the fabricated scaffolds were measured using a tensile test bench (FGS-50E-L, Niece-SHIMPO, Japan). The scaffolds were cut into 5 cm × 1 cm rectangular strips and one end was clamped onto a translational stage while the other end was clamped to a digital force meter (FGP, Niece-SHIMPO, Japan). The samples were uniaxially stretched at 20 mm min^{-1} until failure. The mechanical characteristics including tensile strength (δ), percentage of elongation at break (ϵ), yield strength, and elastic modulus (E) were calculated from the obtained stress-strain data.

2.5. In vitro cell study

Primary adult human dermal fibroblast cells (HDFs, Bioresource Collection and Research Centre, Taiwan) were cultured in growth medium prepared using Dulbecco's Modified Eagle's Medium (DMEM, Sigma Aldrich, Taiwan) supplemented with 10% FBS and 1% penicillin-streptomycin antibiotics (Pen-Strep, Sigma Aldrich, Taiwan). The cells were incubated and grown in a 5% humidified CO_2 atmosphere at 37 °C according to standard protocols. The HDFs were washed twice with 1 × phosphate buffer saline (PBS, Sigma Aldrich, Taiwan) and the growth medium was replaced every two days until the cells reached 90% confluency. The cells were detached from the culture plate with trypsin-EDTA (Sigma Aldrich, Taiwan) and subcultured until passage four, when the cells were harvested for further analysis.

The cytotoxicity of the scaffolds was examined according to the International Standard ISO 10993–5:2009 with adaptations using a cell counting kit-8 (CCK-8, Sigma Aldrich, Taiwan). Before seeding the cell, the scaffolds were sterilized under ultraviolet light for 1 h and then sequentially soaked in 70% ethanol, PBS, and culture medium at 37 °C. The samples were then fitted into 24-well culture plates for cell seeding. The HDFs were seeded onto the scaffolds at a density of 1×10^4 cells per well and cultured under standard culture conditions. The cytotoxicity of the scaffolds was assessed on days 1, 3 and 7 after seeding, by washing the cell-seeded sample with PBS and further incubation with 500 μl of growth medium containing 10% CCK-8 reagent. After 2 h, 100 μl of the medium was withdrawn from each well and transferred to a 96-well plate. A microplate reader (Bio-Rad 680; Bio-Rad, USA) was used to determine the optical density of the samples at 450 nm. A blank consisting of medium without the cells and a control containing medium with only cells without the scaffolds were also prepared. Cytotoxicity was assessed by determining the cell viability percentage using equation (4):

$$Cellviability(\%) : \frac{OD_{test} - OD_{bg}}{OD_{con} - OD_{bg}} \times 100 \tag{4}$$

where OD_{test}, OD_{bg} and OD_{con} represent the absorbance of the test, background, and control samples, respectively.

Cell-scaffold interactions were determined based on fluorescent images by staining the HDFs with fluorescein diacetate (FDA, Sigma Aldrich, Taiwan). The HDFs were washed and incubated in medium containing FDA for 5 min in a dark environment. The medium was then aspirated, and the HDFs were observed under fluorescence microscope (Eclipse Ni–U, Nikon, Japan) equipped with appropriate filters. The cell morphology, in terms of elongation and orientation, was assessed using ImageJ software based on closest fitting ellipse method as described in Ref. [28]. Cell elongation was defined as the ratio of the long and short axis of the cells and referred to as the aspect ratio. Meanwhile, cell orientation was identified as the angle of cell long axis and the direction of the embedded nanofibre.

HDF migration was studied using an in vitro wound healing assay. This involves the creation of a cell-free gap area within the cell monolayer using a 400 μm thick polydimethylsiloxane (PDMS) slab as a physical barrier [40,41]. Firstly, the sterilized samples were fitted in a 24-well plate. The PDMS slab were then placed perpendicularly to the microstructural array direction in the centre the sample to prevent cell attachment at the targeted cell-free gap area, and 1×10^6 of HDFs cells were seeded per well. The seeded cells seated around the PDMS slab and were grown until 90% confluence, after which the PDMS slab was removed with sterile forceps leaving a 400 μm empty region for the cells to migrate into. After 24 h allowing the cells to grow and migrate into the empty region, the cells were stained with FDA and observed under fluorescence microscope. Cell migration in terms of the gap closure area was measured using ImageJ software.

2.6. Hemolysis study

The hemocompatibility of the fabricated scaffolds was tested using anticoagulated rat blood (BioLasco, Taiwan) following the method described in Ref. [42] with slight modification. To begin, 50 mg of the fabricated scaffold was immersed in 5 ml of 0.9% sodium chloride (NaCl) solution at 37 °C for 24 h. PBS and 1% Triton X-100 were also prepared as negative and positive control, respectively. Then, 0.2 ml of the rat blood was added to each sample extract and incubated at 37 °C for 1 h. After incubation, the suspension was centrifuged at 1000 rpm for 10 min. The supernatant (100 μl) was transferred to a 96-well plate and the absorbance was measured at 545 nm with a microplate reader. The rate of hemolysis was calculated using equation (5):

$$Hemolysis\ rate\ (\%) = \frac{OD_S - OD_{NC}}{OD_{PC} - OD_{NC}} \times 100 \tag{5}$$

where OD_S, OD_{NC}, OD_{PC} is the absorbance of the sample, negative control and positive control group, respectively.

2.7. Gentamicin release from the fabricated composite scaffolds

The drug release kinetics from the fabricated scaffolds were investigated using the Franz diffusion technique and gentamicin as a model drug. Dried gentamicin-loaded scaffold was cut into a 15 mm disc-sample and mounted on the donor compartment of the diffusion cell, which was separated from the receptor chamber by a cellulose membrane. The receptor chamber was filled with 6 ml of phosphate buffer solution (pH 7.4), stirred at 100 rpm with a magnetic stirrer and thermoregulated with a water jacket at 37 °C. Periodically, 1 ml aliquot of the release medium was extracted for sampling and instantly replaced with an equal volume of fresh PBS (pre-equilibrated at 37 °C).

The amount of gentamicin released was determined using an indirect spectrometric method and ninhydrin as the derivatising agent since

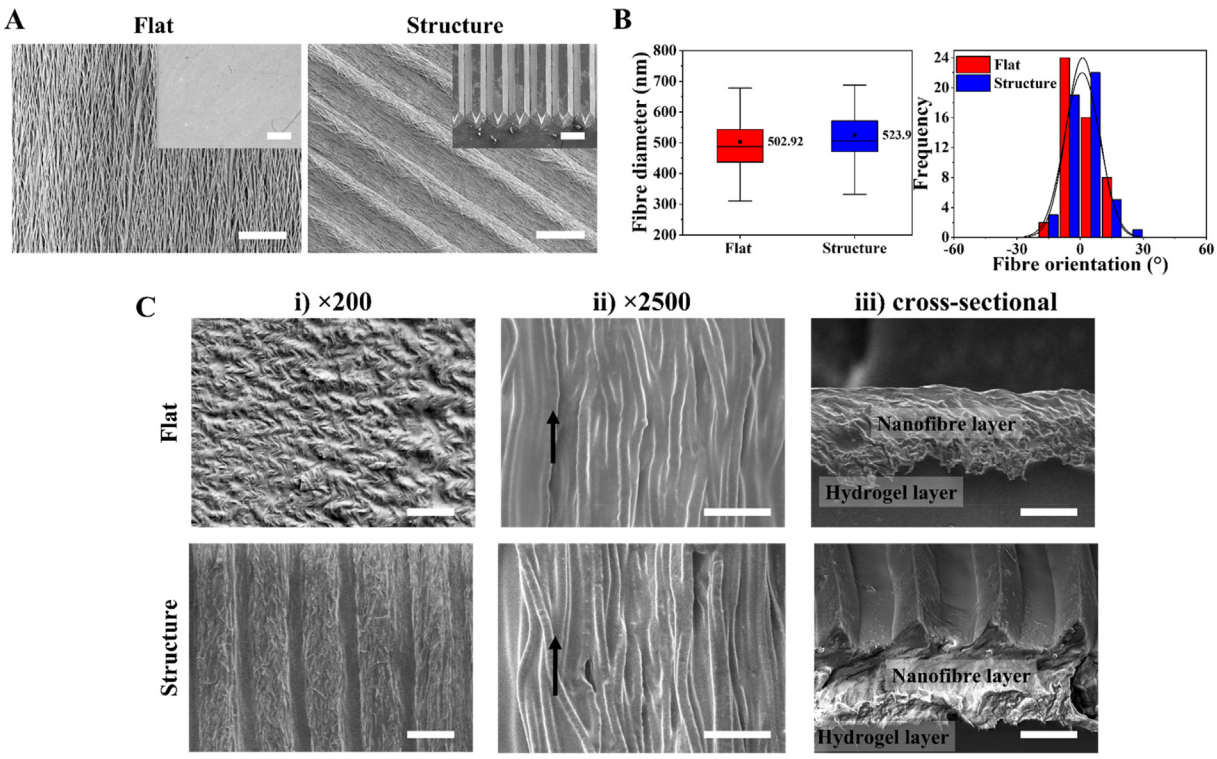

Fig. 2. (A) SEM images of the fabricated nanofibres with flat and structural topography. Insets indicate the Si template used during the centrifugal electrospinning process. Scale bar = 100 μm. (B) Quantitative analysis of the fabricated nanofibre diameter and orientation distribution measured from at least 50 individually fibres. The use of the centrifugal electrospinning machine during nanofibre fabrication produces fibres with consistent diameters and alignments. (C) SEM images of the fabricated nanofibre/hydrogel composite scaffold at (i) lower magnification, scale bar = 200 μm, (ii) higher magnification, scale bar = 10 μm. Black arrows indicate the fibre orientation and (iii) cross-sectional view of the fabricated scaffolds. Scale bar = 100 μm. The combination of nanotopography (nanofibre) and micro-topography (structural microarrays) provides multiscale topographies similar to the extracellular matrix architecture.

gentamicin poorly absorbs UV and visible light [43]. The reaction between ninhydrin and the primary and secondary amines in gentamicin produced purple colour that was easily quantified to establish the gentamicin content by comparison to a standard calibration curve prepared with five known concentrations of gentamicin. The extracted sample was mixed with ninhydrin and placed in water bath (95 °C for 10 min) and cooled in ice water bath to stop the reaction. The absorbance of the samples was measured at 400 nm using UV/Vis spectrophotometer (UV/Vis V-700, Jasco, Taiwan).

2.8. The antibacterial activity of the gentamicin-loaded scaffolds

The antibacterial activity of the gentamicin-loaded scaffolds was evaluated using dynamic contact conditions according to ASTM E2149 [40] against *Staphylococcus aureus* (BCRC 10451, Bioresource Collection and Research Centre, Taiwan) and *Pseudomonas aeruginosa* (BCRC 11633, Bioresource Collection and Research Centre, Taiwan) as representative gram-positive and gram-negative bacteria, respectively. The bacteria were grown overnight in tryptic soy broth to acquire isolated colonies, and then diluted to a viable bacterial suspension containing approximately 10^5 colony-forming units per millilitre (CFU ml^{-1}). For each group, 1 g of sample was added to a flask containing 50 ml of working bacterial suspension and the flasks were shaken in a wrist action shaker at 180 rpm. After 1 h, 100 μl of the bacterial suspension was spread onto a nutrient agar and allowed to grow for another 24 h at 37 °C. The bacteria viability was measured to determine the antibacterial effect of the gentamicin loaded scaffolds.

2.9. In vivo excisional wound model

In vivo wound healing study was conducted using excisional wound on a rat model. The experiment was carried out according to protocols approved by the Institutional Animal Care and Use Committee of National Sun Yat-sen University, Kaohsiung, Taiwan (application no: 10,738). This experiment used 17 healthy adult male Wistar rats weighing around 200–250 g purchased from BioLasco, Taiwan. Before wounding, the dorsum of each rat was shaved, then the skin was excised to create two circular 20 mm diameter full-thickness skin wounds on the back of the rat. The rats were randomly divided into 4 groups, each with 4 rats and one rat remained unwounded was included as control. The scaffolds were applied to cover the excision wounds with the structural surface of the composite scaffold facing the wound site and wrapped with a medical adhesive tape to fix the scaffolds and prevent chewing of the splints. The scaffolds were changed every three days, and photographic images of the wounds were captured using a digital camera during the scaffold-changing process on days 3, 6, 9, 12 and 15 after injury to monitor the healing progress. Throughout the experiment, the rats were housed in micro-isolation cages individually and kept under controlled conditions of humidity (50%–70%), temperature (20 °C–22 °C), light: dark cycle (12 h:12 h), and free access to food and water. The wound healing progress was analysed using ImageJ software and calculated based on the wound reduction area using the following equation (6):

$$Healing\ percentage\ (\%) = \left(\frac{WA_0 - WA_t}{WA_0}\right) \times 100 \quad (6)$$

where WA_0 is the wound area at the wounding day (day 0) and WA_t is the wound area at each respective day.

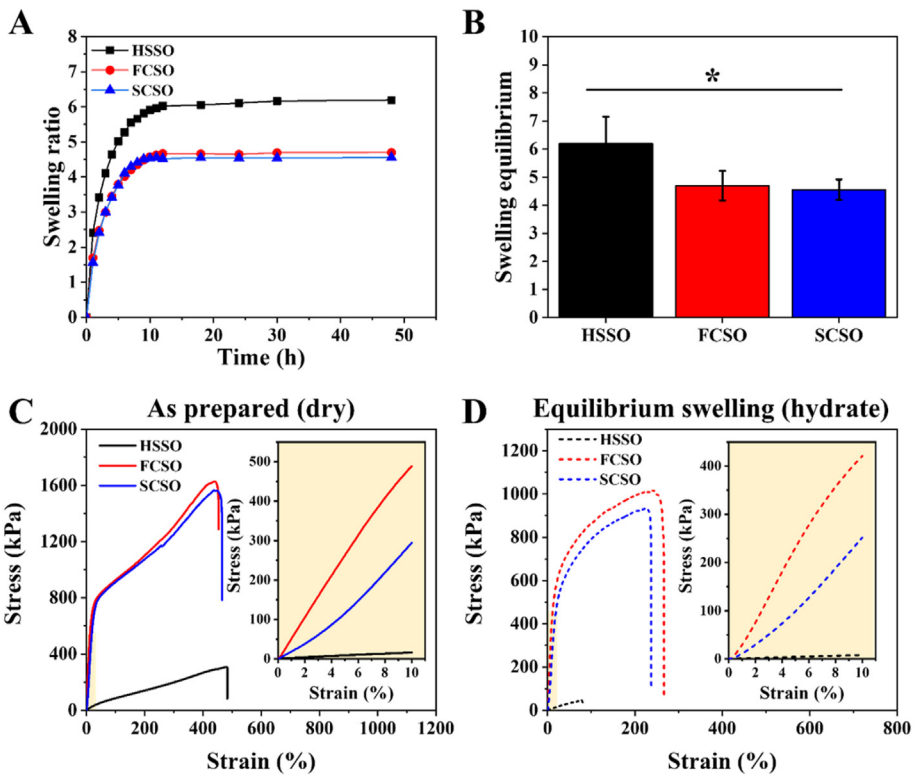

Fig. 3. (A) Swelling kinetics and (B) equilibrium swelling ratios of the pure hydrogel (HSSO), flat composite (FCSO) and structural composite (SCSO) scaffolds at 37 °C in ultrapure water. The results are presented as means ± SD, $n = 5$. Mechanical properties of the fabricated scaffolds. The stress-strain curves of the fabricated scaffolds at (C) as-prepared (dry) and (D) equilibrium swelling at 37 °C (hydrate). The dried scaffolds possessed higher mechanical properties than that the hydrated scaffolds, and the integration of nanofibre layers significantly improves the mechanical properties of the composite scaffolds. The results are presented as means ± SD, $n = 3$, (*p < 0.05 and **p < 0.01 using one-way ANOVA followed by Tukey's post hoc test).

2.10. Histological and immunofluorescent staining

The rats were euthanised at the end of the wound healing study (day 15) and all wound tissues, including the adjacent normal skin (5 mm skin border), were collected for histological analysis. The dissected tissues were fixed for 6 h in 4% paraformaldehyde, then sliced through the widest margin and fixed in the fixing solution overnight [44]. The tissue samples were then dehydrated, diaphanized, wax infiltrated, and embedded in paraffin. To assess the status of the newly regenerated tissues in relation to the administered treatment, the paraffin-embedded tissue samples were sectioned into 5 μm thick sections and stained with hematoxylin and eosin (H&E). A digital slide scanner (MoticEasyScan, Motic, Hong Kong) was used for microscopic observations during the qualitative histological study. The histological state was assessed according to the degree of inflammation, re-epithelialization, and the formation of granulation tissue in the tissue sections.

Immunofluorescence staining of CD31 was carried out to determine wound angiogenesis. Briefly, the paraffined-embedded tissue sections were deparaffinized, rehydrated, and blocked with 5% bovine serum albumin (BSA, Sigma Aldrich Taiwan). The sections were treated overnight at 4 °C with the primary anti-CD31 primary antibody, followed by Alexa Fluor 488 (Sigma Aldrich, Taiwan) secondary antibody for immunostaining. The nuclei were counterstained with 4',6-diamidino-2-phenylindole dihydro-chloride (DAPI, Sigma Aldrich, Taiwan). Quantitative analysis of wound angiogenesis was done by measuring the area of neovascular in the tissue sections.

2.11. Statistical analysis

All the experimental data were presented as means ± standard deviations (SD). One-way analysis of variance (ANOVA) followed by the Tukey post-hoc test was used for the comparison between all groups. Significant difference was indicated with '*' and '**' indicating p value < 0.5 and < 0.01, respectively.

3. Results and discussions

3.1. Characterisation of the fabricated scaffolds

Various methods for manipulating surface topography factors, such as size, alignment, and geometry, to control cell behaviour on biomaterial scaffolds are discussed in the literature. Our previous study demonstrated that a triangular prism geometry had the strongest guiding effect for cell filopodia extension along the triangular apex and became the primary focal point for filopodial protrusion [28]. Accordingly, the surface topography condition of the composite scaffold was engineered with triangular prism microstructures to trigger and guide fibroblast migration to the wound area, thereby accelerate wound closure.

Surface morphology of the fabricated nanofibre meshes and their respective templates used during the spinning process are shown in Fig. 2A. We utilised a non-patterned template to fabricate a flat nanofibre layer and a patterned template with negative triangular prism gratings to generate structural patterns on the nanofibre surface. All spinning procedures were carried out for 2 h under the same conditions, producing nanofibre meshes that were about 600 μm thick. The SEM images showed that the structural patterns were successfully transferred from the template onto the surface of nanofibre mesh with high fidelity. The replicated patterns consisted of triangular prism arrays with structural heights and spacings of 40–60 μm with a fabrication accuracy of 91.44%.

The use of centrifugal electrospinning for fibre fabrication produces nanofibre mesh with a uniform fibre diameter and a high degree of fibre alignment [35]. Fig. 2B shows that the average diameter of the fabricated nanofibres, regardless of the template used, was around 500–700 nm, with an average fibre diameter of 502.92 ± 166 nm and 523.9 ± 100 nm for flat and structural fibres, respectively, similar to the size of the ECM protein networks (50–500 nm). The collected nanofibres were densely packed in a uniaxial arrangement and displayed a narrow orientating deposition on the flat and structural templates, resulting in 88% and 82% of the fibres aligned within 10° from the axial direction, respectively.

To form the composite scaffold, the hydrogel precursor solution was poured onto the fabricated nanofibre and was cross-linked in situ. During gel casting, the solution penetrated through the pores in the nanofibre network and was distributed along the nanofibre surfaces, forming an interface between the two materials. Significant numbers of nanofibre were observed spreading across the top surface of both the flat and structural composite scaffolds, as presented in Fig. 2C(i), confirming the localisation of the nanofibre top layer. Dehydration of the sample caused some structural shrinkage and fibre aggregation during scaffold shrinkage resulted in a rough and wrinkled surface morphology. Direct hydrogel casting has no effect on the morphology of the fabricated fibres, and the surface morphology of the composite scaffolds at higher magnification clearly shows that the fibres maintained in aligned arrangement, as shown in Fig. 2C(ii). Physical interaction between the nanofibre surfaces and the hydrogel network during gelation process produced interlayer adhesion at the interface according to the cross-sectional images in Fig. 2C(iii), indicating good interfacial compatibility was achieved during fabrication. Furthermore, as corroborated from the SEM images, the fabricated pure hydrogel and composite scaffolds was approximately 1 mm thick. Simple linear addition of the nanofibre layers (600 μm for each layer) and hydrogel (1 mm) thickness shows that the thickness of composite scaffold is lower than what would be predicted, indicating an interfaced was formed between these two phases.

The use of different templates had no effect on the formation of the intended scaffold, and the combination of nanofibres and structural patterns produced a nano- and micro-scale topography that resembled multidimensional ECM architectures. The porosity of the aligned PCL nanofibre mesh, pure hydrogel and composite scaffolds is around 83.9%, 92.7% and 72.1%, respectively. The porosity of the composite scaffold is slightly lower in comparison to nanofibre mesh and pure hydrogel scaffolds due to the entanglement of nanofibre and hydrogel networks causes blockage in some pores. Similar trends were reported in previous study stating that the porosity percentage of scaffolds decreases with presence of nanofibre in composite scaffold [45].

Appropriate swelling capacity of the scaffold enables the absorption of wound exudates while maintaining a moist environment around the wound area. Excessive absorption of wound exudate, on the other hand, may result in wound dehydration, which can impede wound contraction and healing. Therefore, determination of the swelling degree is important when developing a scaffold for wound dressing applications. As shown in Fig. 3A, the fabricated scaffolds exhibited a general swelling kinetic pattern characterised by a rapid increase in swelling in the first 24 h, followed by a plateau indicating that equilibrium had been attained. Fig. 3B shows that the equilibrium swelling ratios for HSSO, FCSO and SCSO were calculated as 6.19 ± 0.96, 4.69 ± 0.52 and 4.55 ± 0.36, respectively. The FCSO and SCSO have lower equilibrium swelling by about 1.5-fold ($p < 0.05$) than the HSSO, indicating that the incorporation of hydrophobic PCL nanofibres on the top and bottom layers of the composite scaffold limits the scaffold's swelling ability. The entanglement of nanofibres and the hydrogel polymeric network creates physical cross-linking sites leading to an increase in cross-linking density within the composite scaffold network [46]. Higher cross-linking density impedes the mobility of the polymer chains and thereby restricts the volumetric expansion of the composite scaffolds. The integration of nanofibres also improves the structural integrity of the composite scaffold, preventing dressing fragments from contaminating the wound bed, as well as avoiding undesired wound bed contraction throughout the first stage of healing.

A uniaxial tensile test was conducted to evaluate the mechanical properties of the HSSO, FCSO and SCSO scaffolds in their as-prepared (dry) and equilibrium swelling at 37 °C (hydrated) states. The samples were stretched along the direction of the embedded nanofibre layers for the composite scaffolds. The stress-strain curves of the tested samples are shown in Fig. 3C and D, and their corresponding mechanical characteristics such as tensile strength, percent of elongation, yield strength and elastic modulus are listed in Table 2. The average tensile strength of the as-prepared hydrogel scaffold (HSSO) was relatively weak around 309 kPa, and the presence of integrated nanofibre layers significantly improved the tensile properties of the composite scaffolds, as expected. The tensile strength of the as-prepared composite scaffolds was fivefold greater than that of HSSO, at approximately 1630 kPa for FCSO and 1560 kPa for SCSO, respectively. The composite scaffolds were able to withstand much higher longitudinal stresses, with yield strength increasing from 52 kPa (HSSO) to 792 kPa (FCSO) and 750 kPa (SCSO), and elastic modulus increasing from 115 kPa (HSSO) to 4991 kPa (FCSO) and 2994 kPa (SCSO).

Table 2
The mechanical characteristics and tensile performance of the hydrogel (HSSO), flat composite (FSCO), and structural composite (SCSO) scaffolds at as-prepared (dry) and equilibrium swelling at 37 °C states obtained from their respective stress-strain curves.

Sample	Tensile strength (kPa)		Elongation at break (%)		Yield strength (kPa)		Elastic modulus (kPa)	
	Dry	Swell	Dry	Swell	Dry	Swell	Dry	Swell
HSSO	309	47	483	80	52	24	155	81
FCSO	1630	1015	454	262	792	673	4991	4517
SCSO	1560	933	465	235	750	583	2994	2615

The fabricated scaffolds are more resistant in the dry (as-prepared) than in the hydrated (equilibrium swelling) state, and their respective tensile performance decreases in direct proportion to the water content. High water content in hydrogel network causes the polymer chains to expand, resulting in poor tensile performance. Nonetheless, in an equilibrium state, the composite scaffolds showed similar trends and improvements in tensile properties due to the presence of nanofibre layers. Table 2 shows that the composite scaffolds at equilibrium swelling state had higher tensile strength compared to swelled hydrogel from 47 kPa to approximately 1000 kPa, and thus their percent of elongation, yield strength and elastic modulus from 80% to approximately 200%, 24 kPa–600 kPa and from 81 kPa to 4517 kPa for FCSO and 2615 kPa for SCSO, respectively.

As aforementioned, the integration of nanofibre and hydrogel are based on the physical interaction between nanofibre surface and the hydrogel matrix during gelation process. The interfacial bonds occur through chemical reaction, including hydrogen bond, between the carboxyl and methylene groups of PCL nanofibres and the hydroxyl groups of the PEG-based hydrogel [47–49]. The formation of hydrogen bond between nanofibre surface and hydrogel provides more point-bonded sites in the polymeric backbone, thus the increase in tensile strength. When the composite scaffolds were subjected to an axial tensile load, the load was transferred from the polymer chain to the fibres, preventing the formation of microcracks [7,11,12,46]. The layered arrangement also improved the dimensional stability, resulting in a mechanically stable nanofibre/hydrogel composite network. The overall mechanical properties of the composite scaffolds were not affected by the topography modification from flat to structural, implying that the use of a patterned template during the fabrication processes have negligible effects on the original properties of the fabricated scaffolds.

3.2. Human dermal fibroblast cell responses to the scaffold architecture

Wound dressing scaffolds for tissue engineering applications must be biocompatible and should not exert any toxic effects. CCK-8 reagent assay was used to assess the in vitro cytotoxicity of the fabricated scaffolds by seeding HDF cells directly on the scaffolds and monitoring the HDFs viability up to day 7. Fig. 4A shows that the cells remained viable in all groups throughout the experiment, with viability percentages greater than 80%, indicating that the tested scaffolds were non-toxic to the cells according to the ISO 10993–5:2009 standard [50]. FCSO and SCSO had slightly higher viability percentage than for HSSO, suggesting that the

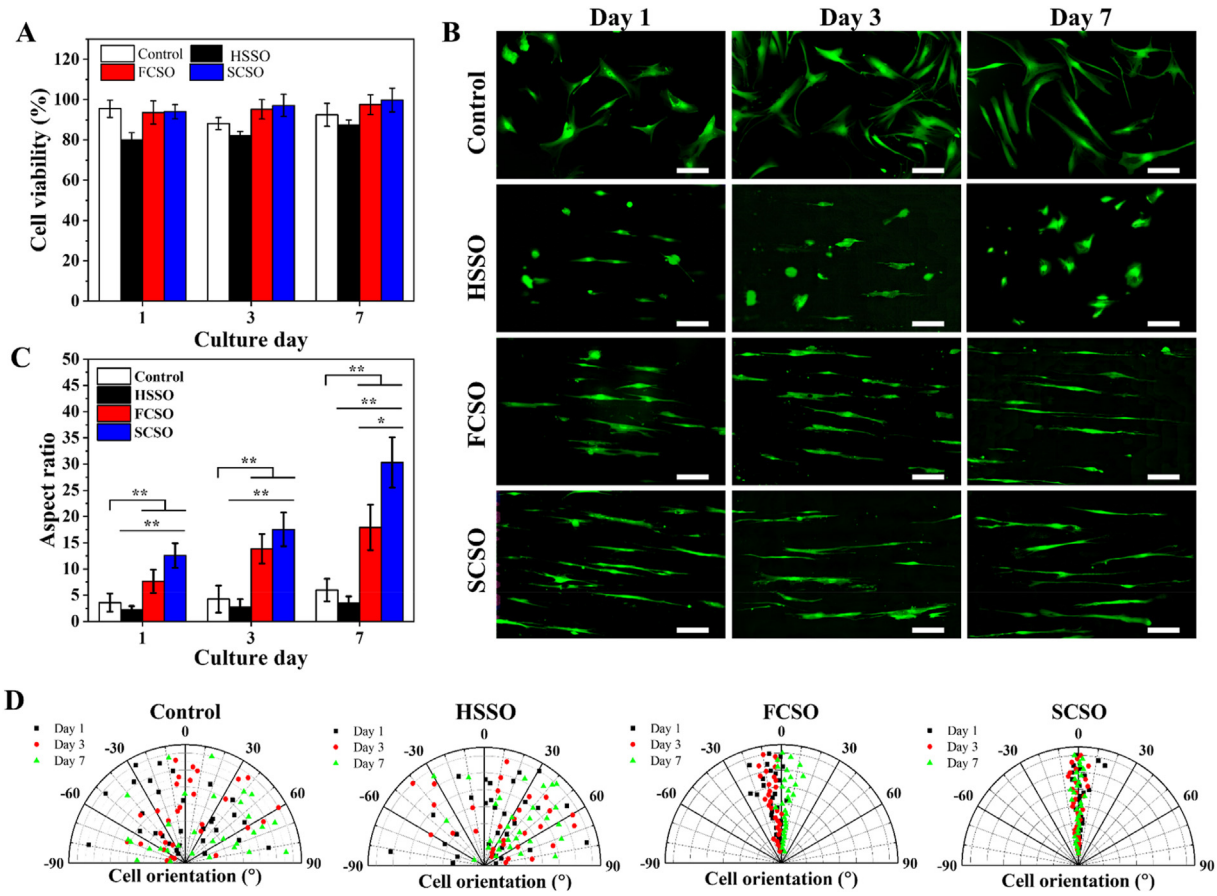

Fig. 4. (A) Result of viability percentage of HDF cells cultured on hydrogel scaffold (HSSO), flat composite scaffold (FCSO) and structural composite scaffold (SCSO) for 7 days. The results are presented as means ± SD, $n = 4$. Overall HDF cell morphology and orientation when cultured on different composite scaffolds for 7 days. (B) Fluorescent images of HDF cells stained with fluorescein diacetate (FDA) at days 1, 3 and 7 of culture. Scale bar = 200 μm. On the composite scaffolds, most cells elongated and showed a preferred alignment along the direction of the incorporated nanofibre. Quantification of the HDF cell (C) elongation index and (D) the scatter data of cell orientation from at least 30 randomly selected cells. The results are presented as means ± SD, $n = 30$, (*$p < 0.05$ and **$p < 0.01$ using one-way ANOVA followed by Tukey's post hoc test).

composite scaffolds could promote HDF proliferation. The composite scaffolds were found to be compatible, therefore suitable for use as wound dressings in practical applications.

The effect of different topography on HDFs responses was also evaluated by fluorescein diacetate (FDA) staining. The overall growth distribution of the HDFs in tissue culture plate (control) showed high activity and spread, as shown in Fig. 4B, with visualisation of a typical spindle shape by day 7. The HDFs cultured on the fabricated scaffolds showed a morphologically distinct phenotype. HDFs on HSSO exhibited a lysed and rounded shape from day 1 and retained the rounded morphology with minimal spreading until day 7. By contrast, HDFs on the composite scaffolds (FCSO and SCSO) revealed a unidirectional elongated shape with obvious filopodial formations. The HDFs on the composite scaffolds also presented a polarised morphology, as the cells consistently aligning in the direction of the incorporated nanofibres. The morphological changes induced by the underlying scaffolds were also quantified based on the elongation and alignment factors, as shown in Fig. 4C and D.

The average aspect ratio of the cells cultured on HSSO showed a minimal increase from 2.29 ± 0.63 to 3.52 ± 1.25 throughout the culture period, which could be due to the soft nature or the flat surface of the hydrogel matrix. On the other hand, continuous elongation was observed for cells cultured on FCSO and SCSO. Cell extension was fourfold greater on SCSO than in the control group ($p < 0.01$) and sixfold greater than on HSSO ($p < 0.01$) as early as day 1 of culture, and the highest aspect ratio of around 30.31 ± 4.79 was reached on day 7. For cells cultured on FCSO, the cell aspect ratios for days 1 and 7 were 7.65 ± 2.22 and 17.93 ± 4.32, respectively.

The relative orientation of the cultured cells was measured to identify cell alignment on the fabricated scaffolds. We observed that cells on control and HSSO scaffold were randomly oriented in arbitrary angles, with the percentage of aligned cells being less than 25%. Cells on the composite scaffolds, by contrast, showed higher alignment with the direction of the embedded nanofibre layer, with the percentages of aligned cells of 80% and 93% for FCSO and SCSO, respectively. These findings suggest that the integration of the nanofibre layer into the composite scaffold promotes cell–scaffold interactions by providing a greater number of contact points available for cell growth and extension. More importantly, engineering the composite scaffold with microstructural patterns that mimicked the geometric features of the ECM resulted in predominantly elongated and aligned cells that grew in a unidirectional manner. The anisotropic morphology of the HDFs on SCSO was a direct result of the multiscale structural cues provided by the embedded nanofibres (nanotopography) and the microstructural pattern (microtopography), recognised as contact guidance.

Fibroblast cell migration plays an important role for effective wound healing since the cells generate traction and contractile forces, which produces ECM proteins for wound contraction. As the HDFs showed elongated and aligned cell organisation on the composite scaffolds, the ability of the composite scaffolds to direct the movement and migration of HDFs was analysed further using an in vitro wound-healing assay (see Section 2.5. Materials and methods). The rate of cell migration was

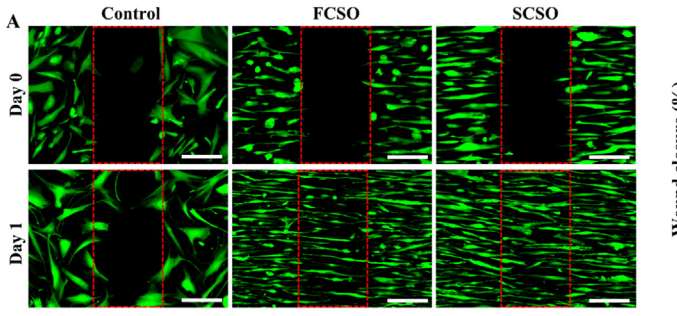

Fig. 5. In vitro wound-healing assay. (A) Fluorescence image of HDF cells on the hydrogel scaffold (HSSO), flat composite scaffold (FCSO) and structural composite scaffold (SCSO) after 1 day. Scale bar = 200 μm. The fluorescence images demonstrated a greater migration of the HDF cells towards the cell-free region with the SCSO than with the control and FCSO scaffolds due to stronger guiding effects provided by the multi-scale topography of SCSO. (B) Quantitative analysis of the percentage of gap closure area after 1 day. The results are presented as means ± SD, $n = 3$, (*$p < 0.05$ and **$p < 0.01$ using one-way ANOVA followed by Tukey's post hoc test).

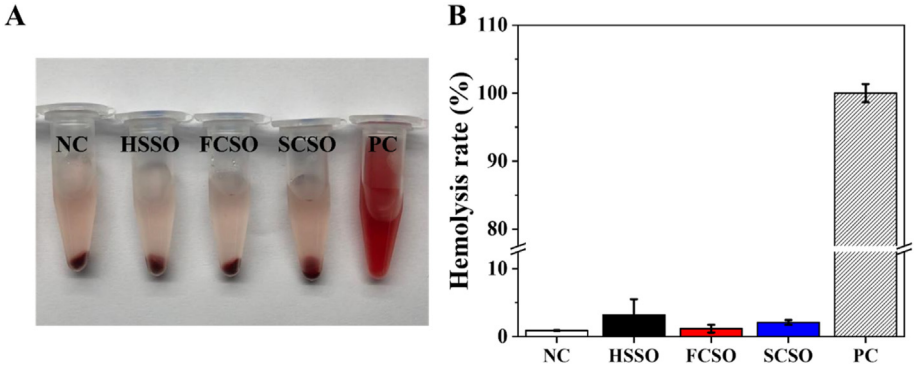

Fig. 6. Hemolysis assay of the hydrogel (HSSO), flat composite (FCSO) and structural composite (SCSO) scaffolds using rat blood. (A) Image of red blood cell after centrifugation. (B) The hemolysis rate after 1 h of incubation at 37 °C. The results are presented as means ± SD, $n = 3$. (For interpretation of the references to colour in this figure legend, the reader is referred to the Web version of this article.)

expressed as the percentage of gap closure and is presented in Fig. 5A.

The cells lining the wound edge actively responded to the newly accessible gap and migrated towards the cell-free area as the healing time progressed. Consistent with the HDF morphology assessment shown in Fig. 5B, the HDFs on the composite scaffolds elongated in consistent alignment which determined the direction of cell migration [51–53]. HDFs migrated in a directional one-way migration towards the centre during the gap closure. This movement was regulated by the contact guidance from the embedded nanofibres. The HDFs migrated much further on SCSO after 24 h ($p < 0.05$) with wound closure of approximately 33.54 ± 1.02% compared to the FCSO (23.52 ± 2.06%) and control (5.57 ± 2.52%) groups. This suggested that the mechanism of gap closure on the SCSO is governed by the activation of lamellipodial protrusions in response to mechanical probing along the microstructural array [53].

Gap closure on SCSO revealed that the cells preferentially crawl and extend lamellipodia on microstructures and head towards the centre of the gap. On FCSO, cells protrusion was also observed, however, the lamellipodial crawling was less prominent and the protrusions were shorter and smaller. Some of the cells were also not oriented in the same direction as the embedded nanofibre. The cells in the control group migrated independently in an uncoordinated manner towards the centre of the gap, hence a minimal cell sheet advance was observed.

3.3. Blood compatibility of the fabricated scaffolds

Good blood compatibility is another important prerequisite of scaffolds as wound dressing since bleeding is inevitable during skin trauma, thus in vitro hemolysis assay was performed to evaluate the blood compatibility of the fabricated scaffolds according to the ASTM F756-17 standard [54]. As observed in Fig. 6A, apparent different in colour were observed between the positive control group and the fabricated scaffold groups. The positive control group (Triton X-100) lysed almost all red blood cells and the supernatant was bright red in colour due to haemoglobin leakage, whereas the supernatant of all scaffolds groups was transparent and nearly colourless, similar to that of the negative control group (PBS). Fig. 6B shows that the hemolysis rate for HSSO, FCSO and SCSO is 3.22%, 1.18% and 2.09%, respectively. Based on the mentioned standard, the hemolysis rates for all samples are below the critical safe value (less than 5%) with HSSO and SCSO showed only slight hemolytic (hemolysis rate between 2% and 5%). The insignificant hemolytic activities of the scaffolds indicate that none of the scaffolds are significantly toxic to red blood cells and are therefore suitable for practical application.

3.4. Gentamicin release from the composite scaffolds

Scaffolds with physical cues alone cannot satisfy the requirements of wound healing. Therefore, to expand the function of the fabricated scaffolds, we loaded gentamicin sulphate, a commonly used aminoglycoside antibiotic for the treatment of superficial skin infections. Gentamicin binds to the bacterial ribosome and inhibits protein synthesis, preventing bacterial growth on wounds and enhancing the therapeutic effect during wound healing. Microbial infection is a common problem in wound management and can lead to delayed healing. Previous studies have discussed the usage of gentamicin as an antibiotic to fight or, at least to prevent wound infection and thus promote healing. In this study, 0.1% gentamicin was loaded into the hydrogel solution and the release of gentamicin was investigated using the Franz diffusion system (see Section 2.7. Materials and methods). Fig. 7A shows the

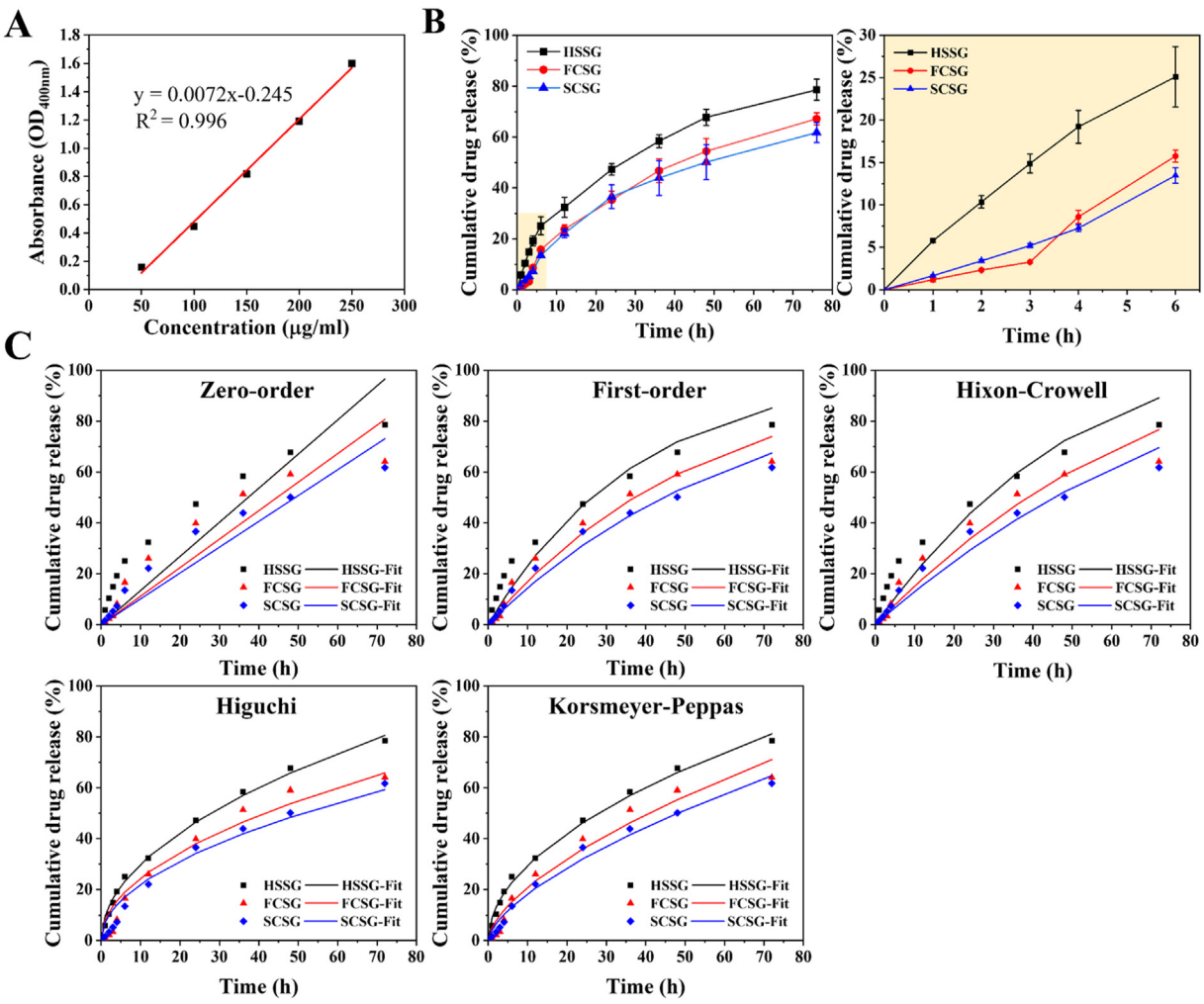

Fig. 7. In vitro gentamicin release from hydrogel (HSSG), flat composite (FCSG) and structural composite (SCSG) scaffolds. (A) The calibration curve for gentamicin sulphate in phosphate buffer solution (pH 7). Cumulative release profiles of gentamicin sulphate (B) full release profile for 3 days and release profile for the first 6 h. The results are presented as means ± SD, $n = 3$. (C) The gentamicin release obtained from the experimental data were fitted into different kinetics models, including zero-order, first-order, Hixon-Crowell, Higuchi and Korsmeyer-Peppas.

standard calibration of five known concentration of ninhydrin-gentamicin complex used for determining the amount of gentamicin release from the composite scaffolds.

Fig. 7B shows that gentamicin release from the hydrogel exhibits a burst release profile, whereas gentamicin released from the composite scaffolds exhibits a slightly delayed release with a more linear release profile. A sharp rise in the cumulative release of gentamicin from HSSG is evident within the first 6 h, with approximately 33% of the gentamicin released in a significant burst, followed by a gradual release of another 45% of the gentamicin from 6 h to 72 h. The composite scaffolds, however, showed a substantially reduced burst effect (about twofold less than HSSG), with approximately 15% of the gentamicin released within the first 6 h. Subsequently, approximately 52% and 48% of gentamicin was released in a more linear and sustained manner from the FCSG and SCSG scaffolds, respectively.

Drug release from the hydrogel matrix is influenced by a swelling-controlled diffusion mechanism, involving simultaneous absorption of the release medium into the hydrogel matrix and the diffusion of the drug through the swollen hydrogel rubbery region into the release medium. These simultaneous actions result in the initial burst release of the drugs. In this regard, the presence of a nanofibre layer in the composite scaffolds acts as the diffusion barrier that controls the mobility of drug molecules and effectively reduces the initial burst release. The additional nanofibre layer also reduced the effective diffusion coefficient and impeded the swelling ability, thereby altering the gentamicin released profile to a sustained release.

Table 3
The kinetics parameters of gentamicin sulphate release from hydrogel (HSSG), flat composite (FCSG) and structural composite (SCSO) scaffolds.

Sample	Zero order		First order		Higuchi		Hixon-Crowell		Korsmeyers-Peppas		
	k_0	R^2	k_1	R^2	k_H	R^2	k_{HC}	R^2	k_{KP}	R^2	n
HSSG	1.341	0.956	0.026	0.992	9.501	0.998	0.007	0.987	9.123	0.997	0.511
FCSG	1.120	0.947	0.019	0.986	7.762	0.984	0.005	0.978	5.019	0.984	0.620
SCSG	1.015	0.966	0.016	0.993	6.988	0.993	0.005	0.986	4.202	0.993	0.640

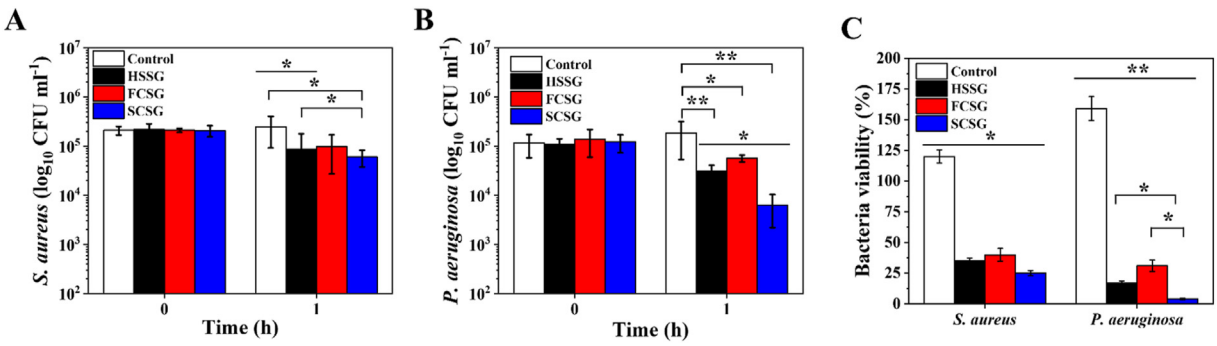

Fig. 8. The in vitro anti-bacterial activity (plots of log 10 CFU ml^{-1}) of the hydrogel (HSSG), flat composite (FCSG) and structural composite (SCSO) scaffolds loaded with gentamicin sulphate against (A) *Staphylococcus aureus* and (B) *Pseudomonas aeruginosa.* (C) The bacteria viability percentage after 1 h treatments with the scaffolds. The results are presented as means ± SD, $n = 3$. (*p < 0.05; **p < 0.01 using one-way ANOVA followed by Tukey's post hoc test).

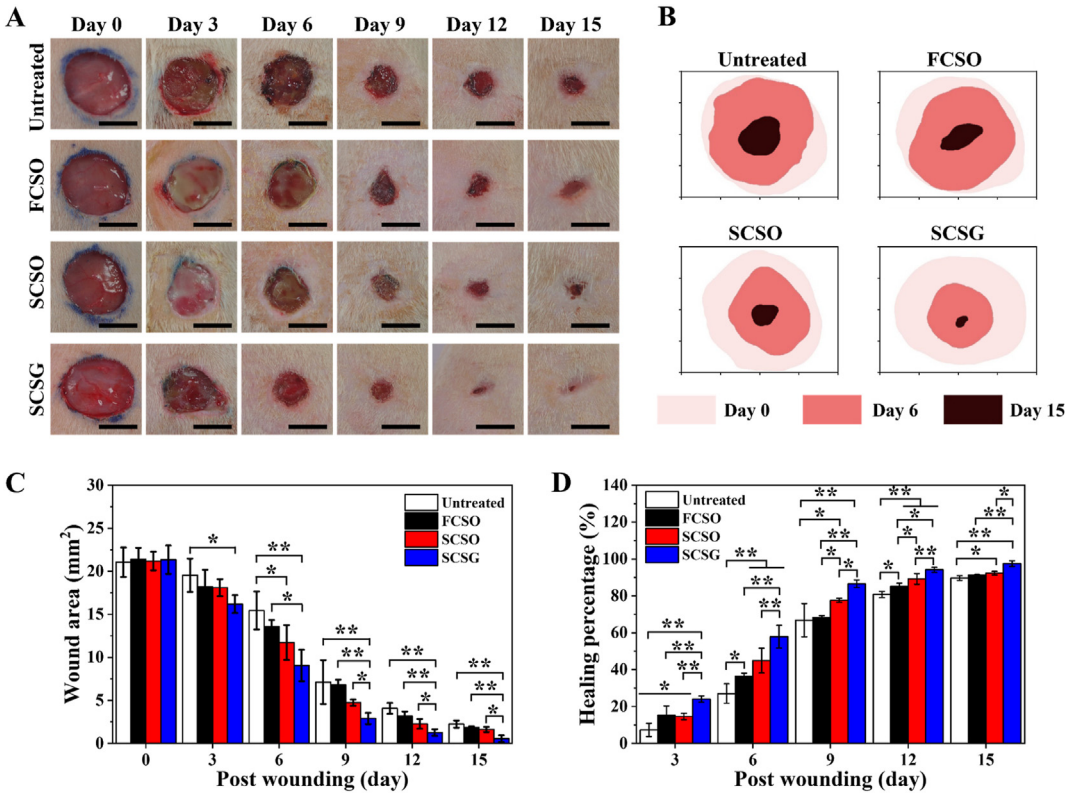

Fig. 9. In vivo wound-healing study using a Wistar rat model of excisional wound-healing. (A) Representative macroscopic images of the wound without treatment (untreated), treatment with a flat composite scaffold, structural composite scaffold and structural composite scaffold loaded with gentamicin at 0, 3, 6-, 9-, 12- and 15-days of healing. Scale bar = 10 mm. (B) The respective wound traces indicate the healing status during the 15 days of the experiment. Quantitative analysis of (C) wound area and (D) wound-healing percentage as a function of time and treatments. The results are presented as means ± SD, $n = 6$. (*p < 0.05; **p < 0.01 using one-way ANOVA followed by Tukey's post hoc test).

The mechanism of gentamicin release from the hydrogel and the composite scaffolds was determined by fitting the experimental release data to five different kinetic models as presented in Fig. 7C. The regression coefficient value (R^2) (Table 3) were calculated to determine the most appropriate model to explain the release kinetics mechanism of gentamicin. The experimental data show that gentamicin release from the hydrogel (HSSG) is best fit to the Korsmeyer-Peppas model (R^2 = 0.997), whereas the composite scaffolds are best fit to the first-order release model (R^2 = 0.986 for FCSG and R^2 = 0.993 for SCSG), implying that the amount of gentamicin released is proportional to the amount of gentamicin concentration remaining in the scaffold. The diffusion exponent (n) according to the Korsmeyer-Peppas model indicated that gentamicin release followed non-Fickian diffusion ($0.45 < n <$ 0.89). The constant k value of the composite scaffolds was also lower than that of the hydrogel. As this value is dependent on the diffusion path length and drug diffusivity, this confirmed that the presence of a nanofibre layer affects the diffusion path length and tortuosity for drug release [9,23].

3.5. Antibacterial activity of the gentamicin-loaded composite scaffolds

The antibacterial activity of the fabricated gentamicin-loaded scaffolds was tested using dynamic contact conditions according to ASTM E2149 against gram-negative *Staphylococcus aureus* and gram-positive *Pseudomonas aeruginosa* bacteria. In this experiment, the bacterial suspensions were treated with the gentamicin-loaded hydrogel (HSSG) and

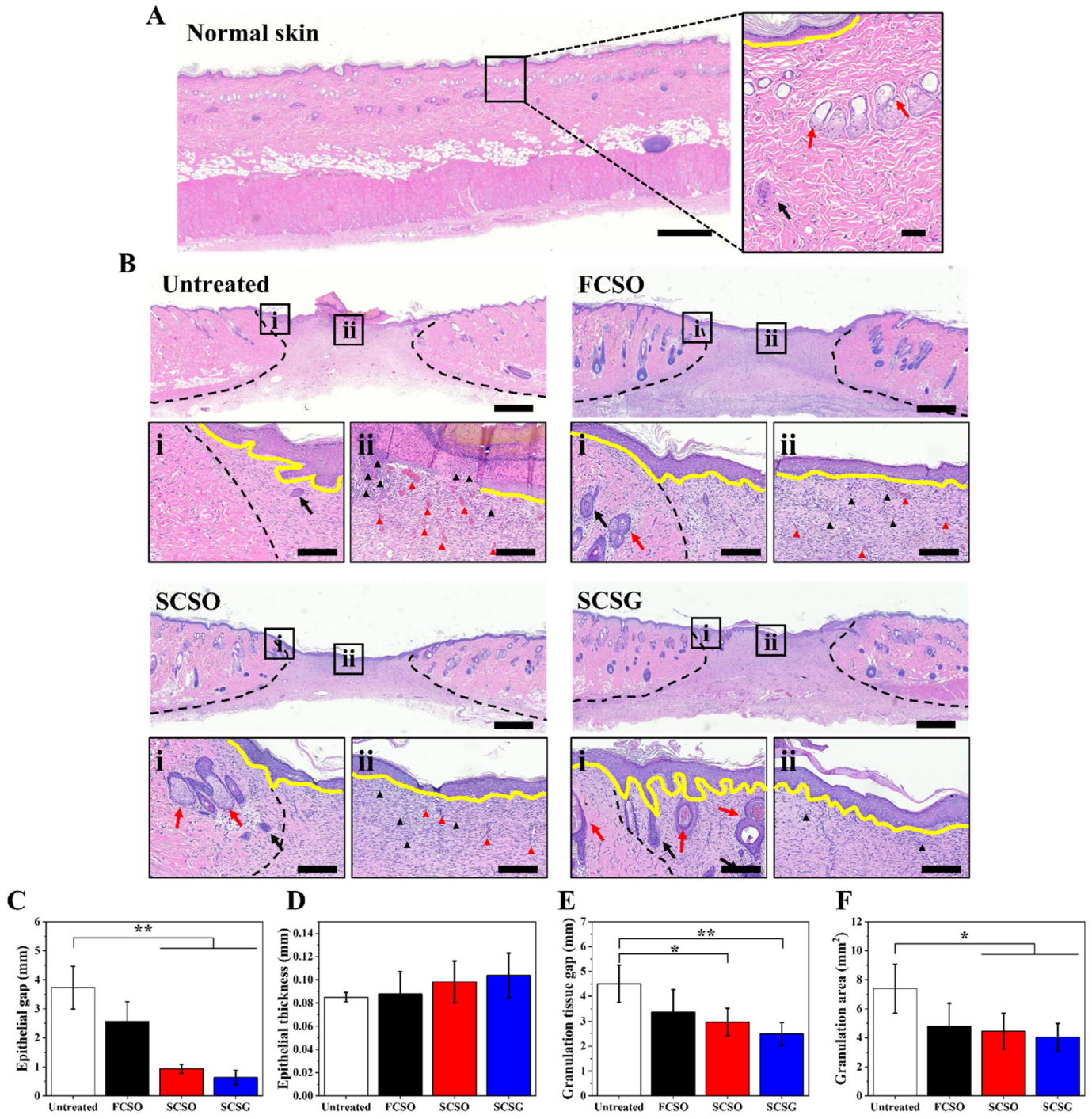

Fig. 10. The histology of excisional wound sections stained with hematoxylin-eosin (H&E) on day 15 after wounding. (A) Normal tissue (healthy, unwounded rat) as reference. (B) H&E-stained images of untreated wound or treated with flat composite scaffold (FCSO), structural composite scaffold (SCSO) and gentamicin-loaded structural composite scaffold (SCSG). Scale bar = 800 μm. The insets indicate the sites of the magnified areas (i) peri-lesion and (ii) intra-lesion. Scale bar = 60 μm. The black dotted lines indicate the wound edge in the healing region. The yellow lines indicate the regenerated epithelial layer. Black and red arrows indicate the sweat glands and hair follicles, respectively. The black and red triangles indicate the inflammatory cells and the blood vessels in the new tissue. Quantitative analysis of the (C) epithelial gap, (D) epithelial thickness, (E) granulation tissue gap as well as (F) granulation tissue area. The results are presented as means ± SD, $n = 6$. (*$p < 0.05$; **$p < 0.01$ using one-way ANOVA followed by Tukey's post hoc test). (For interpretation of the references to colour in this figure legend, the reader is referred to the Web version of this article.)

composite scaffolds (FCSG and SCSG), and the antibacterial activity related to the growth reduction of the bacteria was determined. Fig. 8A and B shows the log reduction of *S. aureus* and *P. aeruginosa* growth after 1 h treatment in comparison to a hydrogel scaffold without gentamicin (HSSO) as a control. No reduction in *S. aureus* and *P. aeruginosa* CFUs was observed in control group, whereas these common pathogen at the wound area were effectively killed with the addition of 0.1% of gentamicin into the fabricated scaffolds as both bacteria showed reduced viability when treated with gentamicin-loaded scaffolds as shown in Fig. 8C. For example, treatment with HSSG reduced *S. aureus* viability by about 65% ($p < 0.05$) and killed 83% ($p < 0.01$) of *P. aeruginosa*. SCSG demonstrated the highest antibacterial activity towards both bacterial

species, leading to reductions of 75% ($p < 0.05$) and 96% ($p < 0.01$) of the *S. aureus* and *P. aeruginosa* bacteria, respectively. Overall, all of the samples showed good antibacterial effects and reduced bacterial level by more than 50%, supporting the potential used of gentamicin-loaded scaffolds as wound dressings. The results also proved that the pharmaceutical function and antibacterial activity of gentamicin were retained when loaded into the scaffolds.

3.6. In vivo excisional wound healing study

A rat excisional wound model was used to evaluate the performance of the fabricated composite scaffold as an actual wound dressing (see Section 2.9. Materials and methods). Fig. 9 shows that the application of composite scaffolds as well as the addition of gentamicin to the composite scaffolds provided therapeutic benefits for wound healing in comparison to the untreated group. As observed in Fig. 9A, most of the wounds exhibited an acute inflammatory phase in the early stages of healing (day 3), during which a localised yellowish slough appeared. The formation of wound scabs was also observed from day 6 and these began to detach as the healing process progressed. However, this state was not evident in the gentamicin-loaded scaffold group (SCSG), primarily due to the antibacterial activity of gentamicin.

The healing percentage was calculated based on the wound reduction area at specific time by tracing the wound area from the macroscopic images using ImageJ software. The wound area for all groups decreased and contracted towards the centre as the healing time progressed (Fig. 9B), and the quantitative analysis revealed that the wound closure accelerated with the scaffold treatment. Fig. 9C and D shows that the SCSG group shows fastest wound closure and highest healing percentage from dah 3 to day 15 than the other group. Wound area of the SCSG group was reduced to 9.06 ± 1.83 mm^2 from the initial wound area within the first 6 days of healing, with a remarkable increase in healing percentage of 57.91% ($p < 0.01$) compared to the other groups. The SCSG group had the greatest healing percentage, followed by the untreated group at 30% (15.44 ± 2.20 mm^2), the FCSO group at 21% (13.58 ± 0.75 mm^2) and the SCSO group at 12% (11.73 ± 2.02 mm^2). After 15 days, the wounds treated with SCSG were almost completely healed, with highest healing percentage of 97.49% (0.56 ± 0.37 mm^2), followed by the SCSO group at 92.38% (1.62 ± 0.30 mm^2) (SCSG and SCSO: $p < 0.05$) the FCSO group at 91.31% (1.85 ± 0.13 mm^2) (SCSG and FCSO: $p < 0.01$) and the untreated group at 89.65% (2.24 ± 0.42 mm^2) (SCSG and untreated: $p < 0.01$).

3.7. Histological assessment

Histological assessments were performed by staining the sample tissue sections with hematoxylin-eosin (H&E). Fig. 10A presents the sample of stained-normal tissue section (unwounded rat) to be used as the reference. The degree of healing was compared at the growing margin of the granulation tissue adjoining the normal skin (i-perilesional site) and the reticular dermal centre of the granulation tissue (ii-intralesional site), as shown in Fig. 10B. The perilesional site showed an increasing number of skin appendages, such as sweat glands (black arrows) and hair follicles (red arrows), in the SCSO and SCSG groups. Few appendages were also found in the granulation tissue area of the SCSG group, indicating faster tissue regeneration than the other groups. These findings are remarkable, as hair follicles are seldom regenerated in the initial stage of healing of a full-thickness skin wound [55].

The extent of wound healing was evaluated based on the inflammatory response, re-epithelialization, and formation of granulation tissue. The earliest responses after skin injury are those associated with the inflammatory reaction. A greater number of inflammatory cells, such as neutrophils, lymphocytes, and plasma cells, accumulate at the wound site during inflammation to fight against invading microorganisms. As the healing process progresses, the proportion of inflammatory cells at the wound site gradually decreases. Although all groups exhibited an acute inflammatory response characterised by distinct polymorphonuclear leukocytes at the intralesional site, H&E-stained images revealed that the wound healing efficacy differed for each group. A higher density of blue-stained inflammatory cells (black triangles) was found in the untreated group, indicating that a moderate inflammatory reaction was still present. By contrast, the inflammation subsided with the scaffold treatment, which resulted in less exudate and fewer inflammatory cells. The SCSG group had the fewest inflammatory traces, possibly due to the anti-inflammatory effects of gentamicin.

Proliferation occurs after the inflammation recedes and leads to re-epithelialization, the formation of granulation tissue and restoration of a vascular network. These restore the structure and function of the wounded skin by replacing the provisional wound matrix formed during haemostasis [56]. During re-epithelialization, the epidermal keratinocytes from the basal layer of the wound edge proliferate, differentiate, and migrate towards the wound area, constructing a new epithelial layer and restoring the skin barrier. The epithelial gap defined as the distance between the advancing edges of epidermis, and the epithelial thickness were used to determine the degree of epithelialization. The quantitative analysis in Fig. 10C indicate that the epidermis in the untreated group was not fully healed, as the wounds revealed partial epithelialization with incomplete closure of the epithelial layer, with average epithelial gap of 3.72 ± 0.73 mm. The wounds in the untreated group were left exposed to the air without treatment causing the cells to dehydrate and die, forming a scab and crust over the wound which impairs re-epithelialization. By contrast, the application of microstructural scaffolds promoted the regeneration of a new epithelial layer, as evidenced by the significant reduction of the epithelial gap. The SCSG group had the smallest average epithelial gap (0.63 ± 0.24 mm) compared to the SCSO group (0.93 ± 0.15 mm). The regenerated epithelial layer in SCSG group is also the thickest (0.10 ± 0.02 mm) compared to other groups (Fig. 10D) with more stratified epithelium indicating better re-epithelialization.

Granulation tissue maturation is another important indicator of wound healing; hence, the gap and the area of the produced granulation tissue were examined. Wounds treated with SCSG had the smallest average granulation tissue gap (2.48 ± 0.46 mm) between the healthy dermis on both sides of the wounds as presented in Fig. 10E, with gap differences of 2.03 ± 0.29 mm ($p < 0.01$) from untreated, 0.89 ± 0.45 mm from FCSO and 0.49 ± 0.10 mm from SCSO. According to Fig. 10F, the SCSG group also had the smallest unhealed wound area, as measured by the granulation tissue area, at about 4.05 ± 0.93 mm^2, significantly smaller than the untreated group (7.39 ± 1.68 mm^2) ($p < 0.05$). Furthermore, in the scaffold treatment groups, the regenerated collagen fibres and fibroblasts under the granulation tissue area appeared more mature, arranged in a horizontal direction in fascicle-to-sheet-like patterns, as opposed to the untreated group, where the fibres and fibroblasts were arranged in a reticular pattern with vertically and horizontally mixed orientations.

During the proliferative stage of angiogenesis, the restoration of new vasculature and capillaries is critical to ensure oxygen and nutrients supply to the growing tissues required for effective wound healing. New capillaries grow at a rapid rate during the early stages of wound healing, resulting in an abundant network of new blood vessels and a vascular bed with denser capillaries than does normal tissue. Wound angiogenesis suppressed gradually when tissue hypoxia is restored, as the level of growth factors in the granulation tissue decreases and the inflammation subsides. This causes the newly formed capillaries to regress and the normal vascular density is restored [57]. Therefore, the evaluation of wound angiogenesis can often be correlated with healing progression. Compared to the normal tissue (unwounded skin) in Fig. 11A, a higher blood vessel density was still visible in the granulation tissue area of wounds in the untreated group (Fig. 11B) at day 15, as reflected by the high CD31 expression. The density of blood vessels in the scaffold treatment groups, on the other hand, is comparable to that of normal tissue, suggesting that the wounds undergo faster healing. Fig. 11C shows

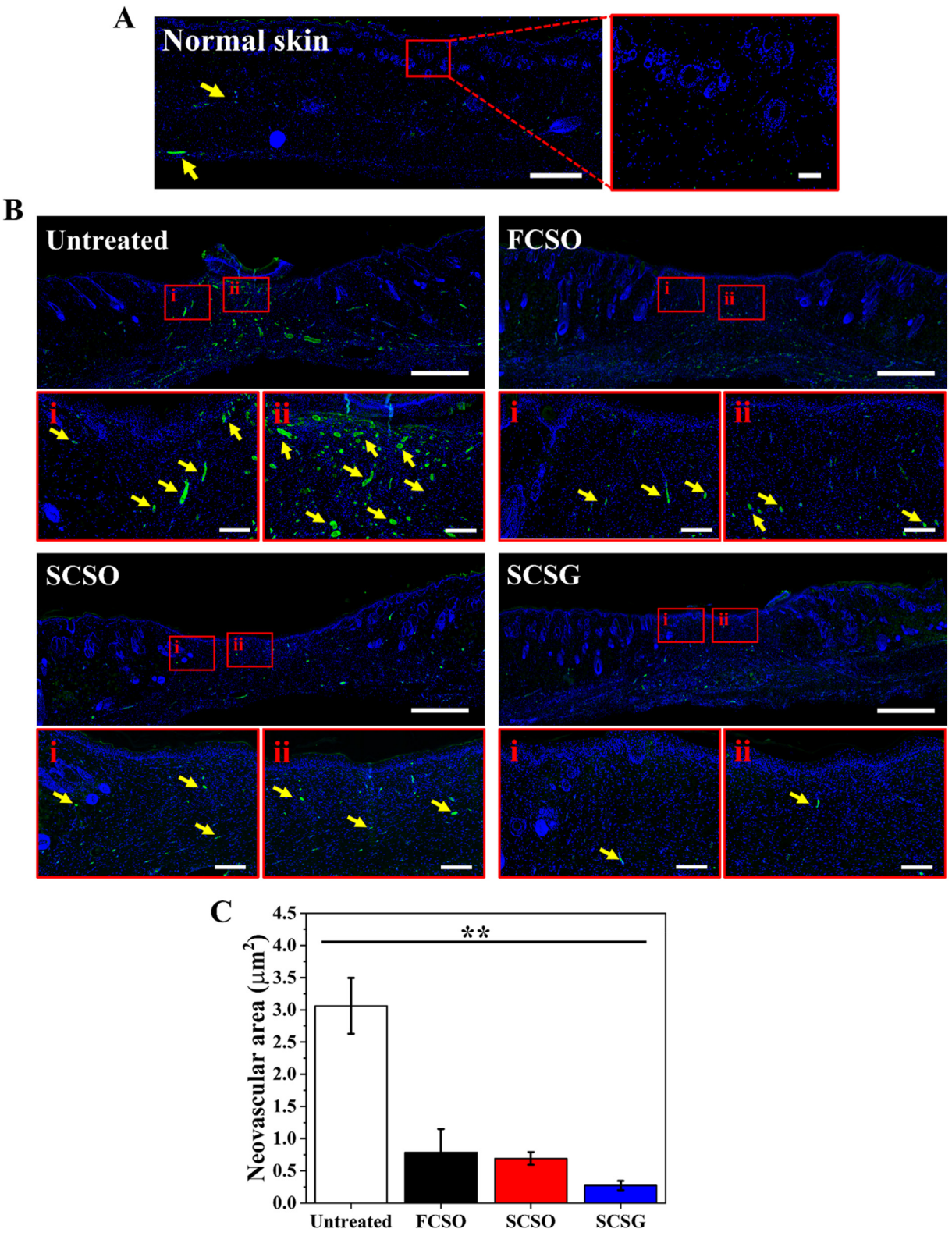

Fig. 11. Expression of the vascular endothelial marker CD31 (green) with nuclei counterstained with DAPI (blue). (A) Normal tissue (healthy, unwounded rat) as reference. (B) CD31 expression for untreated wound or treated with flat composite scaffold (FCSO), structural composite scaffold (SCSO) and gentamicin-loaded structural composite scaffold (SCSG). The neovascularisation (yellow arrows) was lowest in the SCSG group compared to the other groups. Scale bar = 800 μm. The insets indicate the sites of the magnified areas (i) peri-lesion and (ii) intra-lesion. Scale bar = 100 μm. (C) Quantitative analysis of neovascular area measured at the granulation tissue area. (*$p < 0.05$; **$p < 0.01$ using one-way ANOVA followed by Tukey's post hoc test). (For interpretation of the references to colour in this figure legend, the reader is referred to the Web version of this article.)

that the average neovascular area of the scaffold treatment groups is significantly lower ($p < 0.01$) than the untreated group. For instance, the average neovascular area of the SCSG group was approximately 0.27 ± 0.07 μm^2, or about 12-fold lower at day 15 compared to the untreated group.

Taken together, the results indicated better healing of a full-thickness skin wound treated with SCSG at day 15, followed by the SCSO and then the FCSO groups compared to the untreated group. The healing efficacy of the SCSG and SCSO scaffolds was attributed to the scaffold structural topography, which stimulated fibroblast directionality and migration to potentially accelerate wound closure. The SCSG group had the highest healing efficacy, it is reasonable to speculate that the combined effects of structural topography and gentamicin promote wound healing and tissue regeneration, particularly in the early stages of healing, due largely to the ability of gentamicin to modulate the wound inflammatory environment.

4. Conclusion

A nanofibre/hydrogel composite scaffold was successfully fabricated by integrating highly aligned nanofibres on the top and bottom surfaces of a hydrogel layer intended as a wound dressing. The porosity and the swelling ability of the composite scaffold decreases with the presence of nanofibre layers. The composite scaffold showed a significantly higher tensile strength up to 1560 kPa, 465% of elongation, and a yield strength of approximately 750 kPa due to the interfacial bonding between the nanofibre surface and the hydrogel network. Two engineering strategies were applied to improve the bio-functionality of the composite scaffold including: generating microstructural arrays on the surface of the nanofibre top layer to regulate cell behaviour and loading gentamicin into the hydrogel middle layer to provide antibacterial activity. The multidimensional surface provided by the structural composite scaffold modulated fibroblast cells to develop longer filopodial protrusions and achieved the highest aspect ratio of approximately 30.31 compared to a flat composite scaffold where the cells elongated to 17.93. The in vitro wound healing study found that consistent alignment of fibroblast cells on the structural composite scaffold guided cell migration, with the cells stretching further over the wound site to cover 33.54% of the wound gap, potentially accelerating wound closure. Hemolysis rate of the structural composite scaffold is 2.09%, which is lower than the critical value set according to the standard, proving that the scaffold is safe for practical applications. Gentamicin-loaded composite scaffolds killed more than 50% of *S. aureus* and *P. aeruginosa* bacteria, confirming good antibacterial activity of the scaffolds. The application of a gentamicin-loaded structural composite scaffold as an excisional wound treatment resulted in healing of 97.49% of the wound area, and histological examination revealed less inflammation, a smaller epithelial gap and granulation tissue area, indicating faster healing progression. Overall, the findings provide good insights for the development of multifunctional composite scaffolds to promote wound healing.

Data availability statement

Not applicable.

Credit author statement contribution

N.A.M.R. involves in the methodology, investigation, formal analysis, and writing and editing the original draft. W.-C.L. contributed to the resources, supervision, funding acquisition, and review and editing the original draft. All authors have read and agreed to the published version of the manuscript.

Declaration of competing interest

The authors declare that they have no known competing financial interests or personal relationships that could have appeared to influence the work reported in this paper.

Acknowledgements

This work was supported by the Ministry of Science and Technology, Taiwan [MOST110-2221-E-110-066-MY2]. The authors acknowledge the facilities and resources provided by Biomimicking and Engineering Lab (BEing^2 Lab), National Sun Yat-sen University, Taiwan throughout the research.

References

[1] Q. Fu, C. Duan, Z. Yan, Y. Li, Y. Si, L. Liu, J. Yu, B. Ding, Nanofiber-based hydrogels: controllable synthesis and multifunctional applications, Macromol, Rapid Commun. 39 (2018), 1800058, https://doi.org/10.1002/marc.201800058.

[2] F. Afghah, N.B. Iyison, A. Nadernezhad, A. Midi, O. Sen, B. Saner Okan, M. Culha, B. Koc, 3D Fiber reinforced hydrogel scaffolds by melt electrowriting and gel casting as a hybrid design for wound healing, Adv. Healthc. Mater. (2022), 2102068, https://doi.org/10.1002/adhm.202102068.

[3] X. Zhao, M. Ding, C. Xu, X. Zhang, S. Liu, X. Lin, L. Wang, Y. Xia, A self-reinforcing strategy enables the intimate interface for anisotropic alginate composite hydrogels, Carbohydr. Polym. 251 (2021), 117054, https://doi.org/10.1016/j.carbpol.2020.117054.

[4] A. Thorvaldsson, J. Silva-Correia, J.M. Oliveira, R.L. Reis, P. Gatenholm, P. Walkenström, Development of nanofiber-reinforced hydrogel scaffolds for nucleus pulposus regeneration by a combination of electrospinning and spraying technique, J. Appl. Polym. Sci. 128 (2013) 1158–1163, https://doi.org/10.1002/app.38316.

[5] M. Llorens-Gámez, B. Salesa, Á. Serrano-Aroca, Physical and biological properties of alginate/carbon nanofibers hydrogel films, Int. J. Biol. Macromol. 151 (2020) 499–507, https://doi.org/10.1016/j.ijbiomac.2020.02.213.

[6] W. Qiu, H. Han, M. Li, N. Li, Q. Wang, X. Qin, X. Wang, J. Yu, Y. Zhou, Y. Li, F. Li, D. Wu, Nanofibers reinforced injectable hydrogel with self-healing, antibacterial, and hemostatic properties for chronic wound healing, J. Colloid Interface Sci. 596 (2021) 312–323, https://doi.org/10.1016/j.jcis.2021.02.107.

[7] Y. Huang, X. Li, Z. Lu, H. Zhang, J. Huang, K. Yan, D. Wang, Nanofiber-reinforced bulk hydrogel: preparation and structural, mechanical, and biological properties, J. Mater. Chem. B. 8 (2020) 9794–9803, https://doi.org/10.1039/D0TB01948H.

[8] Y. Chen, Y. Qiu, Q. Wang, D. Li, T. Hussain, H. Ke, Q. Wei, Mussel-inspired sandwich-like nanofibers/hydrogel composite with super adhesive, sustained drug release and anti-infection capacity, Chem. Eng. J. 399 (2020), 125668, https://doi.org/10.1016/j.cej.2020.125668.

[9] P. Zare, M. Pezeshki-Modaress, S.M. Davachi, P. Zare, F. Yazdian, S. Simorgh, H. Ghanbari, H. Rashedi, Z. Bagher, Alginate sulfate-based hydrogel/nanofiber composite scaffold with controlled Kartogenin delivery for tissue engineering, Carbohydr. Polym. 266 (2021), 118123, https://doi.org/10.1016/j.carbpol.2021.118123.

[10] H.-Y. Mi, Y. Jiang, X. Jing, E. Enriquez, H. Li, Q. Li, L.-S. Turng, Fabrication of triple-layered vascular grafts composed of silk fibers, polyacrylamide hydrogel, and polyurethane nanofibers with biomimetic mechanical properties, Mater. Sci. Eng. C 98 (2019) 241–249, https://doi.org/10.1016/j.msec.2018.12.126.

[11] Q. He, Z. Wang, Y. Yan, J. Zheng, S. Cai, Polymer nanofiber reinforced double network gel composite: strong, tough and transparent, Extrem. Mech. Lett. 9 (2016) 165–170, https://doi.org/10.1016/j.eml.2016.06.004.

[12] K. Tonsomboon, A.L. Butcher, M.L. Oyen, Strong and tough nanofibrous hydrogel composites based on biomimetic principles, Mater. Sci. Eng. C 72 (2017) 220–227, https://doi.org/10.1016/j.msec.2016.11.025.

[13] H.J. Lee, Y.H. Park, W.-G. Koh, Fabrication of nanofiber microarchitectures localized within hydrogel microparticles and their application to protein delivery and cell encapsulation, Adv. Funct. Mater. 23 (2013) 591–597, https://doi.org/10.1002/adfm.201201501.

[14] O. Bas, E.M. De-Juan-Pardo, M.P. Chhaya, F.M. Wunner, J.E. Jeon, T.J. Klein, D.W. Hutmacher, Enhancing structural integrity of hydrogels by using highly organised melt electrospun fibre constructs, Eur. Polym. J. 72 (2015) 451–463, https://doi.org/10.1016/j.eurpolymj.2015.07.034.

[15] R. Li, J. Lin, Y. Fang, C. Yu, J. Zhang, Y. Xue, Z. Liu, J. Zhang, C. Tang, Y. Huang, Porous boron nitride nanofibers/PVA hydrogels with improved mechanical property and thermal stability, Ceram. Int. 44 (2018) 22439–22444, https://doi.org/10.1016/j.ceramint.2018.09.011.

[16] F. Mirahmadi, M. Tafazzoli-Shadpour, M.A. Shokrgozar, S. Bonakdar, Enhanced mechanical properties of thermosensitive chitosan hydrogel by silk fibers for

cartilage tissue engineering, Mater. Sci. Eng. C 33 (2013) 4786–4794, https://doi.org/10.1016/j.msec.2013.07.043.
[17] S. Khorshidi, A. Karkhaneh, A review on gradient hydrogel/fiber scaffolds for osteochondral regeneration, J. Tissue Eng. Regen. Med. 12 (2018), e1974, https://doi.org/10.1002/term.2628. –e1990.
[18] P.I. Lee, Kinetics of drug release from hydrogel matrices, J. Contr. Release 2 (1985) 277–288, https://doi.org/10.1016/0168-3659(85)90051-3.
[19] D. Caccavo, S. Cascone, G. Lamberti, A.A. Barba, Modeling the drug release from hydrogel-based matrices, Mol. Pharm. 12 (2015) 474–483, https://doi.org/10.1021/mp500563n.
[20] X. Huang, C.S. Brazel, On the importance and mechanisms of burst release in matrix-controlled drug delivery systems, J. Contr. Release 73 (2001) 121–136, https://doi.org/10.1016/S0168-3659(01)00248-6.
[21] S.W. Kim, Y.H. Bae, T. Okano, Hydrogels: swelling, drug loading, and release, Pharm. Res. (N. Y.) 9 (1992) 283–290, https://doi.org/10.1023/a:1015887213431.
[22] R. Wu, R.A. Niamat, B. Sansbury, M. Borjigin, Fabrication and evaluation of multilayer nanofiber-hydrogel meshes with a controlled release property, Fibers 3 (2015) 296–308, https://doi.org/10.3390/fib3030296.
[23] N. Han, J. Johnson, J.J. Lannutti, J.O. Winter, Hydrogel–electrospun fiber composite materials for hydrophilic protein release, J. Contr. Release 158 (2012) 165–170, https://doi.org/10.1016/j.jconrel.2011.09.094.
[24] I.A. Janson, A.J. Putnam, Extracellular matrix elasticity and topography: material-based cues that affect cell function via conserved mechanisms, J. Biomed. Mater. Res., Part A 103 (2015) 1246–1258, https://doi.org/10.1002/jbm.a.35254.
[25] D.-H. Kim, K. Han, K. Gupta, K.W. Kwon, K.-Y. Suh, A. Levchenko, Mechanosensitivity of fibroblast cell shape and movement to anisotropic substratum topography gradients, Biomaterials 30 (2009) 5433–5444, https://doi.org/10.1016/j.biomaterials.2009.06.042.
[26] S. Chen, Y. Guo, R. Liu, S. Wu, J. Fang, B. Huang, Z. Li, Z. Chen, Z. Chen, Tuning surface properties of bone biomaterials to manipulate osteoblastic cell adhesion and the signaling pathways for the enhancement of early osseointegration, Colloids Surf. B Biointerfaces 164 (2018) 58–69, https://doi.org/10.1016/j.colsurfb.2018.01.022.
[27] C.J. Bettinger, R. Langer, J.T. Borenstein, Engineering substrate topography at the micro- and nanoscale to control cell function, Angew. Chem. Int. Ed. 48 (2009) 5406–5415, https://doi.org/10.1002/anie.200805179.
[28] N.A. Mohd Razali, W.-C. Lin, N.A. Norzain, Z.-W. Yu, Controlling cell elongation and orientation by using microstructural nanofibre scaffolds for accelerating tissue regeneration, Mater. Sci. Eng. C 128 (2021), 112321, https://doi.org/10.1016/j.msec.2021.112321.
[29] C.C. Berry, G. Campbell, A. Spadiccino, M. Robertson, A.S.G. Curtis, The influence of microscale topography on fibroblast attachment and motility, Biomaterials 25 (2004) 5781–5788, https://doi.org/10.1016/j.biomaterials.2004.01.029.
[30] G.-J.A. Ter Boo, D. Arens, W.-J. Metsemakers, S. Zeiter, R.G. Richards, D.W. Grijpma, D. Eglin, T.F. Moriarty, Injectable gentamicin-loaded thermo-responsive hyaluronic acid derivative prevents infection in a rabbit model, Acta Biomater. 43 (2016) 185–194, https://doi.org/10.1016/j.actbio.2016.07.029.
[31] R. Dorati, A. De Trizio, I. Genta, A. Merelli, T. Modena, B. Conti, Gentamicin-loaded thermosetting hydrogel and moldable composite scaffold: formulation study and biologic evaluation, J. Pharmacol. Sci. 106 (2017) 1596–1607, https://doi.org/10.1016/j.xphs.2017.02.031.
[32] H.R. Bakhsheshi-Rad, Z. Hadisi, A.F. Ismail, M. Aziz, M. Akbari, F. Berto, X.B. Chen, In vitro and in vivo evaluation of chitosan-alginate/gentamicin wound dressing nanofibrous with high antibacterial performance, Polym. Test. 82 (2020), 106298, https://doi.org/10.1016/j.polymertesting.2019.106298.
[33] F. Ahadi, S. Khorshidi, A. Karkhaneh, A hydrogel/fiber scaffold based on silk fibroin/oxidized pectin with sustainable release of vancomycin hydrochloride, Eur. Polym. J. 118 (2019) 265–274, https://doi.org/10.1016/j.eurpolymj.2019.06.001.
[34] M. Naeimi, R. Tajedin, F. Farahmandfar, M. Naeimi, M. Monajjemi, Preparation and characterization of vancomycin-loaded chitosan/PVA/PEG hydrogels for wound dressing, Mater. Res. Express 7 (2020), 95401, https://doi.org/10.1088/2053-1591/abb154.
[35] N.A. Norzain, W.C. Lin, Orientated and diameter-controlled fibrous scaffolds fabricated using the centrifugal electrospinning technique for stimulating the behaviours of fibroblast cells, J. Ind. Textil. (2021) 1–25, https://doi.org/10.1177/1528083720988127.
[36] H. Chen, Y.S. Lui, Z.W. Tan, J.Y.H. Lee, N.S. Tan, L.P. Tan, Migration and phenotype control of human dermal fibroblasts by electrospun fibrous substrates, Adv. Healthc. Mater. 8 (2019), 1801378, https://doi.org/10.1002/adhm.201801378.
[37] C.-H. Hsieh, N.A. Mohd Razali, W.-C. Lin, Z.-W. Yu, D. Istiqomah, Y. Kotsuchibashi, H.-H. Su, Development of thermo-responsive polycaprolactone–polydimethylsiloxane shrinkable nanofibre mesh, Nanomaterials 10 (1–13) (2020) 1427, https://doi.org/10.3390/nano10071427.
[38] S. Xu, L. Deng, J. Zhang, L. Yin, A. Dong, Composites of electrospun-fibers and hydrogels: a potential solution to current challenges in biological and biomedical field, J. Biomed. Mater. Res. Part B Appl. Biomater. 104 (2016) 640–656, https://doi.org/10.1002/jbm.b.33420.
[39] A. Lopez Marquez, I.E. Gareis, F.J. Dias, C. Gerhard, M.F. Lezcano, Methods to characterize electrospun scaffold morphology: a critical review, Polymers 14 (2022), https://doi.org/10.3390/polym14030467.
[40] R. Riahi, Y. Yang, D.D. Zhang, P.K. Wong, Advances in wound-healing assays for probing collective cell migration, J. Lab. Autom. 17 (2012) 59–65, https://doi.org/10.1177/2211068211426550.
[41] H.N. Kim, Y. Hong, M.S. Kim, S.M. Kim, K.-Y. Suh, Effect of orientation and density of nanotopography in dermal wound healing, Biomaterials 33 (2012) 8782–8792, https://doi.org/10.1016/j.biomaterials.2012.08.038.
[42] H.Y. Zhou, Y.P. Zhang, W.F. Zhang, X.G. Chen, Biocompatibility and characteristics of injectable chitosan-based thermosensitive hydrogel for drug delivery, Carbohydr. Polym. 83 (2011) 1643–1651, https://doi.org/10.1016/j.carbpol.2010.10.022.
[43] A.F.H. Ismail, F. Mohamed, L.M.M. Rosli, M.A.M. Shafri, M.S. Haris, A.B. Adina, Spectrophotometric determination of gentamicin loaded PLGA microparticles and method validation via ninhydrin-gentamicin complex as a rapid quantification approach, J. Appl. Pharmaceut. Sci. 6 (2016) 7–14.
[44] J.J. Mendes, C.I. Leandro, D.P. Bonaparte, A.L. Pinto, A rat model of diabetic wound infection for the evaluation of topical antimicrobial therapies, Comp. Med. 62 (2012) 37–48.
[45] Z. Hadisi, J. Nourmohammadi, J. Mohammadi, Composite of porous starch-silk fibroin nanofiber-calcium phosphate for bone regeneration, Ceram. Int. 41 (2015) 10745–10754, https://doi.org/10.1016/j.ceramint.2015.05.010.
[46] K.J. De France, E.D. Cranston, T. Hoare, Mechanically reinforced injectable hydrogels, ACS Appl. Polym. Mater. 2 (2020) 1016–1030, https://doi.org/10.1021/acsapm.9b00981.
[47] J.-K. Kim, Y.-W. Mai, Y.-W. Mai, Characterization of interfaces, in: Eng. Interfaces Fiber Reinf. Compos., Elsevier Science Ltd, Oxford, 1998, pp. 5–41, https://doi.org/10.1016/B978-008042695-2/50003-8.
[48] S. Jiang, Y. Chen, G. Duan, C. Mei, A. Greiner, S. Agarwal, Electrospun nanofiber reinforced composites: a review, Polym. Chem. 9 (2018) 2685–2720, https://doi.org/10.1039/C8PY00378E.
[49] S. Huang, Q. Fu, L. Yan, B. Kasal, Characterization of interfacial properties between fibre and polymer matrix in composite materials – a critical review, J. Mater. Res. Technol. 13 (2021) 1441–1484, https://doi.org/10.1016/j.jmrt.2021.05.076.
[50] ISO10993-5, Biological evaluation of medical devices-Part 5: tests for in vitro cytotoxicity, in: Int. Organ. Stand., ISO Geneva, Geneva, Switzerland, 2009.
[51] D.-H. Kim, C.-H. Seo, K. Han, K.W. Kwon, A. Levchenko, K.-Y. Suh, Guided cell migration on microtextured substrates with variable local density and anisotropy, Adv. Funct. Mater. 19 (2009) 1579–1586, https://doi.org/10.1002/adfm.200801174.
[52] D.-H. Kim, P.P. Provenzano, C.L. Smith, A. Levchenko, Matrix nanotopography as a regulator of cell function, J. Cell Biol. 197 (2012) 351, https://doi.org/10.1083/jcb.201108062.
[53] G. Charras, E. Sahai, Physical influences of the extracellular environment on cell migration, Nat. Rev. Mol. Cell Biol. 15 (2014) 813–824, https://doi.org/10.1038/nrm3897.
[54] F.756-00 Astm, in: B. Annu, ASTM (Eds.), Standard Practice for Assessment of Hemolytic Properties of Materials, Am. Soc. Test. Mater., Philadelphia, PA, 2000, https://doi.org/10.1520/F0756-13.
[55] S.-H. Chen, C.-T. Tsao, C.-H. Chang, Y.-T. Lai, M.-F. Wu, C.-N. Chuang, H.-C. Chou, C.-K. Wang, K.-H. Hsieh, Assessment of reinforced poly(ethylene glycol) chitosan hydrogels as dressings in a mouse skin wound defect model, Mater. Sci. Eng. C 33 (2013) 2584–2594, https://doi.org/10.1016/j.msec.2013.02.031.
[56] N.X. Landén, D. Li, M. Ståhle, Transition from inflammation to proliferation: a critical step during wound healing, Cell. Mol. Life Sci. 73 (2016) 3861–3885, https://doi.org/10.1007/s00018-016-2268-0.
[57] L.A. DiPietro, Angiogenesis and wound repair: when enough is enough, J. Leukoc. Biol. 100 (2016) 979–984, https://doi.org/10.1189/jlb.4MR0316-102R.